Experimental characterization of the injected mass variation in a high-pressure GDI injector operating with a multiple injection strategy

Published Version:
Viscione, D., Brancaleoni, P.P., Silvagni, G., Ravaglioli, V., Bianchi, G.M., Moro, D., et al. (2023). Experimental characterization of the injected mass variation in a high-pressure GDI injector operating with a multiple injection strategy. INTERNATIONAL JOURNAL OF ENGINE RESEARCH, 25(4), 1-16 [10.1177/14680874231201263].

Availability:
This version is available at: https://hdl.handle.net/11585/957853 since: 2024-05-03

Published:
DOI: http://doi.org/10.1177/14680874231201263

(Article begins on next page)

EXPERIMENTAL CHARACTERIZATION OF THE INJECTED MASS VARIATION IN A HIGH-PRESSURE GDI INJECTOR OPERATING WITH A MULTIPLE INJECTION STRATEGY

Journal:	*International Journal of Engine Research*
Manuscript ID	IJER-23-0150.R1
Manuscript Type:	Standard Article
Date Submitted by the Author:	24-Aug-2023
Complete List of Authors:	Viscione, Davide; Alma Mater Studiorum Università di Bologna, DIN - Department of Industrial Engineering Brancaleoni, Pier Paolo; Alma Mater Studiorum University of Bologna, DIN - Department of Industrial Engineering Silvagni, Giacomo; University of Bologna, DIN - Department of Industrial Engineering RAVAGLIOLI, VITTORIO; University of Bologna, DIN - Department of Industrial Engineering Bianchi, Gian Marco; University of Bologna, DIEM Moro, Davide; Alma Mater Studiorum University of Bologna, DIN - Department of Industrial Engineering De Cesare, Matteo; Marelli Europe S.p.A. Stola, Federico; Marelli Europe S.p.A.,
Keywords:	GDI System, Multiple Injections, Residual Magnetization, Injected Fuel Mass Variation, Control-Oriented Modelling
Abstract:	Increasingly stringent limits to pollutants released by Internal Combustion Engines pushed the automotive research to develop technologies to reduce fuel consumption and emissions. Higher injection pressures are beneficial to accelerate the atomization phase, reducing the particulate matter and unburned hydrocarbon emissions. However, the spray protrusion inside the combustion chamber is enhanced and, consequently, the generation of a thick wall film, which tends to increase the latter emissions. Thus, multiple-injection strategies might be beneficial for both the atomization rate and the spray penetration, owing to a stratified charge inside the chamber. This paper investigates the effect of the adoption of multiple-injection

strategies on the behaviour of a GDI injector operating in high injection pressure conditions. The resulting injected mass is influenced by electrical phenomena on the excitation circuit, which mainly depend on the relative time between the end of the first injection and the start of the following. Hence, the total amount of fuel injected with the multiple-injection pattern will differ from its nominal value. In this work, a specific experimental layout was developed to characterize the behaviour of the injector in different operating conditions and quantify the deviation between actual and nominal injected mass. The impact of the magnetized coils on the overall injected mass has been captured referring to the modification of the shape of the driving current profile with respect to the nominal one. Then, a correlation which considers the electric charge variation on the coils has been implemented to model the phenomenon and, consequently, to counterbalance the electro-magnetic effect on the injected mass. The resulting strategy successfully allowed to reduce the difference between the actual and target fuel mass from up to 30% to almost 5%, owing to its implementation on the injection control system to automatically correct the injection commands and compensate the fuel mass deviations.

EXPERIMENTAL CHARACTERIZATION OF THE INJECTED MASS VARIATION IN A HIGH-PRESSURE GDI INJECTOR OPERATING WITH A MULTIPLE INJECTION STRATEGY

Davide Viscione, Pier Paolo Brancaleoni, Giacomo Silvagni, Vittorio Ravaglioli, Gian Marco Bianchi, Davide Moro

DIN – Dipartimento di Ingegneria Industriale, Alma Mater Studiorum – Università di Bologna, Bologna, 40136 Italy

davide.viscione2@unibo.it; pier.brancaleoni2@unibo.it; giacomo.silvagni2@unibo.it; vittorio.ravaglioli2@unibo.it; gianmarco.bianchi@unibo.it; davide.moro@unibo.it

Matteo De Cesare, Federico Stola

Marelli Europe SpA

Matteo.Decesare@marelli.com; Federico.Stola@marelli.com

CORRESPONDING AUTHOR

Davide Viscione, davide.viscione2@unibo.it, DIN – Dipartimento di Ingegneria Industriale, Alma Mater Studiorum – Università di Bologna, Bologna, 40136 Italy

ABSTRACT

Increasingly stringent limits to pollutants released by Internal Combustion Engines pushed the automotive research to develop technologies to reduce fuel consumption and emissions. Higher injection pressures are beneficial to accelerate the atomization phase, reducing the particulate matter and unburned hydrocarbon emissions. However, the spray protrusion inside the combustion chamber is enhanced and, consequently, the generation of a thick wall film, which tends to increase the latter emissions. Thus, multiple-injection strategies might be beneficial for both the atomization rate and the spray penetration, owing to a stratified charge inside the chamber.

This paper investigates the effect of the adoption of multiple-injection strategies on the behaviour of a GDI injector operating in high injection pressure conditions. The resulting injected mass is influenced by electrical phenomena on the excitation circuit, which mainly depend on the relative time between the end of the first injection and the start of the following. Hence, the total amount of fuel injected with the multiple-injection pattern will differ from its nominal value. In this work, a specific experimental layout was developed to characterize the behaviour of the injector in different operating conditions and quantify the deviation between actual and nominal injected mass. The impact of the magnetized coils on the overall injected mass has been captured referring to the modification of the shape of the driving current profile with respect to the nominal one. Then, a correlation which considers the electric charge variation on the coils has been implemented to model the phenomenon and, consequently, to counterbalance the electro-magnetic effect on the injected mass. The resulting strategy successfully allowed to reduce the difference between the actual and target fuel mass from up to 30% to almost 5%, owing to its implementation on the injection control system to automatically correct the injection commands and compensate the fuel mass deviations.

KEYWORDS

- GDI System
- Multiple Injections
- Residual Magnetization
- Injected Fuel Mass Variation
- Control-Oriented Modelling

SYMBOLS/ABBREVIATIONS

A_1	Electric charge on the injection coil in magnetized conditions
A_2	Electric charge on the injection coil in unmagnetized conditions
A_3	Difference between magnetized and unmagnetized electric charge
CCV	Cycle-to-Cycle Variability
DI	Direct Injection
DT	Dwell Time
dt	Time differential
ECU	Electronic Control Unit
EOI	End Of Injection
$ET_{corrected}$	Corrected Energizing Time to compensate the magnetization phenomenon
ET_{eq}	Equivalent Energizing Time due to the magnetization phenomenon
ET_1	Energizing Time of the first injection pulse
ET_2	Energizing Time of the second injection pulse
Ipeak	Normalized current peak
Ihold	Normalized current hold
GCI	Gasoline Compression Ignition
GDI	Gasoline Direct Injection
GPF	Gasoline Particulate Filter
HP	High Pressure
i(t)	Current behavior in time
ICE	Internal Combustion Engine
LP	Low Pressure
LTC	Low Temperature Combustion
MPROP	Magnetic Proportional
PFI	Port Fuel Injection
PM	Particulate Matter
PWM	Pulse Width Modulation
Q	Electric charge on the injector coil
RCP	Rapid Control Prototyping
RON	Research Octane Number
RPM	Revolution Per Minute
SA	Spark Advance
SACI	Spark Assisted Compression Ignition
SNR	Signal to Noise Ratio
SOI	Start Of Injection
UHC	Unburnt Hydrocarbon
ΔET	Variation of Energizing Time due to the magnetization phenomenon

INTRODUCTION

Over the pasts years, modern regulations for the limitation of the amount of pollutants emitted by an Internal Combustion Engine (ICE) forced the researchers to develop new technical solutions. Regarding gasoline engines, the introduction of Direct Injection (DI) systems allowed the reduction of the knock tendency and, consequently, the achievement of higher efficiencies (more advanced Spark Advance (SA) can be applied, mainly because of the reduced temperature inside the chamber, [1]). On the other hand, several studies reported a correlation between the adoption of a GDI (Gasoline Direct Injection) system and the increase of Particulate

Matter (PM) and Unburned Hydrocarbon (UHC) emissions [2-4]. In fact, compared to a conventional Port Fuel Injection (PFI) engine, the fuel injected by a GDI system has less time to be optimally mixed with air, generating very rich local regions, which are less favoured to be oxidised. Moreover, depending on the injection pressure and timing, defined by the Start of Injection (SOI), small liquid droplets and liquid film on the walls might be generated, leading to PM formation during the combustion process [5]. Thus, even for gasoline engines, modern emission regulations forced to install a dedicated after-treatment system, the Gasoline Particulate Filter (GPF), to comply with the imposed limits. Mamakos et al. [6] demonstrated that the introduction of a supplementary element in the exhaust system results in higher hardware cost and backpressure, reducing the performance of the engine (especially efficiency). To enhance the atomization rate and, consequently, the mixing process, working on the injection strategy might be effective to mitigate the emissions. Increasing the injection pressure and optimizing the SOI [7, 8] could be beneficial to obtain smaller droplets, improve quality and homogeneity of the air-fuel mixture and mitigate the interaction between the liquid jets and the walls of the combustion chamber, owing to a thinner wall film. An excessive increase of the injection pressure leads to a faster atomization rate, but it could generate a greater spray protrusion inside the combustion chamber, leading to the generation of wall film. Moreover, especially considering noticeable engine operations such as cold starts and/or catalyst heating, high injection pressure might even reduce the performance of the engine. As reported in the literature [9], the combination of low temperature and low volumetric efficiency has a negative impact on the mixing process and contributes to the production of wall film. For this reason, to take into account both effects, Zheng et al. [10] indicated that a multiple injection strategy is potentially effective to mitigate the creation of a wall film. Furthermore, depending on the SOI of the second injection, an increase of turbulence kinetic energy around the spark plug in correspondence of the SA can be induced, owing to a reduction of the Cycle-to-Cycle Variability (CCV) [11, 12]. A multiple injection strategy is particularly effective for the application of innovative combustion concepts such as Low-Temperature Combustion (LTC), in which pollutants reduction and efficiency increase can be achieved directly working on combustion physics and combining the benefits of both spark-ignited and compression-ignited engines [13]. Zhou et al. [14] evidenced that the adoption of a multiple injection strategy in a high compression ratio gasoline engine is also useful to improve the performance of Spark-Assisted Compression Ignition (SACI) combustion. As a matter of fact, depending on the SOI of the second injection, that induces a local fuel stratification around the spark plug, the knock onset can be mitigated accelerating the turbulent flame speed and reducing the fuel mass fraction which undergoes to auto-ignition. Similarly, Cho et al. [15] highlighted that the fuel stratification strategy plays a fundamental role on the control of the autoignition mechanism in Gasoline Compression Ignition (GCI) concepts. In fact, as Liu et al. [16] demonstrated, the engine performance for a GCI engine is strongly affected by thermodynamic mixture conditions. Ravaglioli et al. [17] declared that, without modifying the engine hardware, GCI combustion has the potential to increase the engine-out performance for medium-high load operations only by working on the injection pattern and strategy.

Since the efficiency improvement associated to LTC combustions depends on the local mixture conditions, all the above discussed combustion methodologies require a robust control of the amount of fuel injected. Unfortunately, similarly to conventional high-pressure Common-Rail systems, for which the well-known pressure wave propagation phenomenon induced by the first injection influences the mass injected in the subsequent ones [18, 19], also GDI systems, operating with closely spaced injections, might suffer from deviations in the injected fuel mass. Cavicchi et al. [20] noted that the injected fuel deviation from the nominal quantity derives from the combination of two effects: the first one is associated to an electromagnetic phenomenon located in the injector coil, while the second one is given by the pressure wave propagation in the injection system. The electromagnetic phenomenon is related to the residual magnetization energy of the coil in the secondary circuit, which is provided by the excitation current for the first injection. As a consequence, in correspondence of the SOI of the second injection, an acceleration of the opening phase of the injector needle is induced, owing to a greater injected mass with respect to the nominal requested quantity. However, such electrical phenomenon has been scarcely investigated in the literature. Moreover, a compensation of such electrical phenomenon might be potentially effective for the fuel economy improvement and the reduction of pollutant emissions.

In the present paper, the influence of the electromagnetic phenomenon on the fuel injected mass is investigated for a GDI injection system which is capable to deliver gasoline at pressures up to 750 bar. In particular, the deviation from the fuel nominal quantity has been characterized as a function of the injection pressure and the time interval between the end of the first injection and the start of the second pulse (Dwell Time, DT). The investigation has been carried out also varying the duration of each injection command (Energizing Time, ET), which directly influences the residual magnetization energy. Then, focusing on the variation of shape of the excitation current profiles, a zero-dimensional model which estimates the injected mass considering the magnetization effect has been developed and validated, comparing the simulated results with the experimental measurements. Finally, the model has been inverted to predict the ET correction necessary to compensate the electromagnetic effect. To validate the control-oriented inverted model, the developed strategy has been implemented in a fully programmable rapid control prototyping system and used for the real-time calculation of the injection pattern. The analysis of the experimental results proved that the accuracy obtained using the proposed correction methodology is compatible with the requirements of on-board application.

EXPERIMENTAL SETUP

The experimental campaign has been conducted using a specifically designed hydraulic flow test bench for high-pressure injection system [21]. In this case, the layout has been slightly modified to test a high-pressure fuel system with GDI injectors provided by Marelli Europe SpA. A schematic of the hydraulic flow test bench system is shown in Figure 1. The test bench has been fuelled with commercial Research Octane Number (RON) 95 gasoline and the fuel consumption has been measured by using an AVL Balance 733s. A mechanical pressure regulator, located between the Low-Pressure (LP) and High-Pressure (HP) pump, allows keeping at approximately 4.5 bar the pressure in correspondence of the intake of the HP pump (nominal operating condition for the HP system). To control the desired pressure in the rail, a normally opened solenoid metering valve (MPROP) has been adopted to adjust the fuel flow on the return line of the HP pump. To avoid an excessive increase of gasoline temperature, a water-cooled heat exchanger has been installed in the return line between the LP pump and the AVL Balance, which kept the fuel temperature close to the ambient temperature.

[Insert Figure 1]

Figure 1: Schematic of the flushing bench system.

To investigate the injector behaviour and have a robust control of the test operations, additional sensors, such as standard sensors for pressure and temperature, have been installed on both the LP and HP sides of the circuit. To detect the variations on the current driving profile provided by the electromagnetic effect, the current clamp Hioki CT6846A has been located in correspondence of the primary coil of the injector. Moreover, to measure the pump rotational speed, an optical encoder has been mounted on the pump shaft. Finally, two high-pressure piezoresistive pressure sensors Kistler 4067A have been mounted on the fuel feed duct, one close to the injector and the other one to the rail (Figure 2), the goal being to acquire the instantaneous pressure traces during the injection events collecting the enough data to analyse the effect of the pressure wave propagation on the injected fuel mass (this phenomenon will be investigated in a future paper).

[Insert Figure 2]

Figure 2: Sensors on the HP system. In particular, the two Kistler sensors have been located at the beginning and at the end of the HP duct between the rail and the injector.

A Rapid Control Prototyping (RCP) system based on National Instruments cRIO 9082 developed on LabView environment has been specifically designed to manage both data acquisition flushing bench. The acquisition frequencies for each signal have been chosen to maintain the main carriers of the injection system significantly below the Nyquist frequency [22]. For instance, regarding the signals coming from the feed duct on the HP side, a sampling frequency of 100 kHz has been selected to collect the pressure fluctuations. To control the rail pressure, the HP Bosch pump has been mechanically connected to an electric motor (5.5 kW maximum power at 3000 rpm) using a toothed belt. The transmission ratio between the electric motor and the HP pump has been imposed to 0.5 to simulate the rotational speeds characteristic of the HP pump in its on-board installation. During all the tests, the rotational speed of the HP pump has been set at approximately 500 rpm, obtained directly controlling a dedicated inverter connected to the electric motor. Based on the measured rail pressure, the RCP system has been able to control the MPROP opening percentage through a calibrated Pulse-Width-Modulation (PWM) controller. In this way, it has been possible to keep the fuel pressure at its target value during each test.

The whole injection pattern (number of injections, ET, and DT) has been designed and managed using a fully programmable Electronic Control Unit (ECU) (SPARK by Alma Automotive), which allows overcoming the limitations usually present when a production ECU with standard control software is used with custom injection patterns. The injection parameters set in the ECU have been logged, during each test, using INCA software. The adopted injection system is able to faithfully replicate the nominal injector control conditions compared to the standard production application. Figure 3 shows the test bench control layout and the integration between the RCP system and SPARK ECU.

[Insert Figure 3]

Figure 3: Scheme of flushing bench acquisition and control.

Bearing in mind that the AVL balance is not sensitive to small fuel variations, the duration of each experimental acquisition with the system running at stationary conditions has been kept longer than 2 minutes to reduce the measurement errors in the evaluation of the fuel consumption, and the injected mass per cycle has been calculated dividing the whole mass injected during the test by the number of cycles.

EXPERIMENTAL ACTIVITY

This section highlights the procedures used to analyse the injected mass variation caused by the residual magnetization phenomenon in the injector coils, running with a multiple injection strategy.

i) Injector hydraulic characterization

The first objective of the experimental campaign has been the characterization of the hydraulic response of the injector in the case of a single injection pulse. Details on the test conditions can be found in Table 1.

Table 1: Operating conditions.

Ambient Pressure [bar]	Ambient Temperature [°C]	Injector Energizing Time [μs]	Injection Pressure [bar]
1	20	350:100:1950	200:100:700
			750

For each imposed pressure in the rail, experimental tests have been conducted varying the ET and collecting the overall mass variation coming from the signal of the AVL balance system. Then, the injected mass per shot has been computed knowing both test duration and injection frequency, which has been fixed by the rotational speed of the HP pump. In the presented layout, the injected fuel is released directly in a constant-volume chamber at the ambient pressure. Figure 4 shows the results provided by the tests. It is important to underline that, for the injectors under study, the range at which the injected fuel mass experiences low repeatability (i.e., the ballistic operation range), changes depending on the injection pressure, as highlighted in Figure 4 and reported in [23].

[Insert Figure 4]

Figure 4: Injected mass with respect to the ET at different injection pressures.

In particular, the higher the pressure, the higher the minimum ET at which the injector does not operate in the ballistic region. For the highest tested injection pressure, fixed at 750 bar in this work, the transition from the ballistic operation takes place at almost 700 μs.

Conversely, the injector response in the case of ETs out of the ballistic operation is linear for each injection pressure investigated. Figure 5 collects the results highlighted in Figure 4, generating the injector map, which will be used later. It is important to mention that since the injector needle is directly opened by the electromagnetic force induced by the injector coils, the injector driving profile (standard peak and hold driving profile) has to be changed following the specifications provided by the injection system manufacturer. As a consequence, due to the correlation between higher injection pressure and the increased current needed to raise the needle and open the injector, the electrical peak and hold characteristic parameters, i.e., peak (Ipeak) and hold (Ihold) current, have been adapted for each injection pressure. Table 2 shows the injector driving current parameters as a function of the injection pressure normalized with respect to the maximum current value reported in the injector datasheet for the highest working pressure of the injector (750 bar).

Table 2: Normalized injector driving current parameters, Ipeak and Ihold, as a function of the injection pressure: 100% represent the working current of the injector for each parameter.

Injection Pressure [bar]	**Normalized Ipeak [%]**	**Normalized Ihold [%]**
50	50	29
100	50	32
200	54	33
300	58	34
400	65	35
500	74	42
600	85	50
700	100	62
750	100	62

[Insert Figure 5]

Figure 5: Single pulse injector map.

To better clarify this aspect, Figure 6 reports the shapes of the injector current driving profiles for two different injection pressure normalized with respect to the maximum working current of the injector for each parameter. As it can be noticed, even though the ET has been kept constant between the two profiles, the current amplitude (both in peak and hold values) is significantly different. Since the use of unnecessary high current can increase

217 the temperature of both the coil and the injector, different driving current profiles enhance reliability and durability of the injector.

219 [Insert Figure 6]

220 *Figure 6: Variation of the current driving profiles shape at different injection pressure and equal ET.*

221 As a result, based on the operating injection pressure, the ECU continuously adjusts the injector driving profile according to the interpolation of Table 2.

223 **ii) Injector behaviour during multiple injection operations**

224 Once the injector behaviour has been characterized, determining the injector map for a single pulse, the following step of the activity consisted in the analysis of closely spaced pulses, initially investigated fixing the ET for both injections at 700 μs. To highlight the impact of electromagnetic phenomena in case of closely spaced injection pulses (in a wide range of injection pressures) this fixed value of ET has been selected, avoiding uncertainties that might be due to the operation in the ballistic region. Tests have been conducted relying on the conditions listed in Table 3.

230 *Table 3: Tests conditions in multiple injection operations.*

ET 1 [μs]	ET 2 [μs]	Injection Pressure [bar]	Dwell Time [μs]
700	700	300:200:700	50:50:1500
			1600:100:2000
			2250:250:4000

231

232 For each condition, the DT between the two injections has been progressively increased and the obtained results are summarized in Figure 7.

234 [Insert Figure 7]

235 *Figure 7: Injected mass variation as a function of the DT between two consecutive injections with ET = 700 μs.*

236 Figure 7 shows the total amount of injected mass per cycle. For all the injection pressures investigated, different behaviors can be noticed at different values of DT. In particular, the injected mass remains approximately stable between 1500 μs and 4000 μs. Conversely, moving from extremely close injections (DT = 50 μs) towards slightly higher DT values, a maximum amount of injected mass is reached. In this condition, the two injections are hydraulically overlapped, meaning that the needle has not reached yet its seat while it has to

open again for the second pulse. In particular, the higher the injection pressure, the narrower is the hydraulic overlapping phase, since the needle experiences a greater closing force provided directly by the rail pressure [19, 23]. The DT at which the maximum value of fuel injected can be found is the one at which the proximity of the current profiles leads to the maximum duration of needle opening (at 700 bar for example, as clearly visible in Figure 8, for very small dwell times, e.g., 50 □s, the partial overlap of the current profiles leads to a reduction of the injected mass from the peak value, approximately located at 200 □s). The behaviour of the injector in the intermediate region (between the peak of injected mass and DT equal to 1500 μs) can be understood observing Figure 8 and Figure 9, where the driving current profiles applied to the primary injector coil are compared while the DT is varied.

[Insert Figure 8]

Figure 8: Mean current driving profiles in the injector coils synchronized at SOI_1*.*

To give a comprehensive view of the electromagnetic phenomenon, the shapes of the driving profiles are shown in Figure 8 synchronized with respect to the SOI of the first injection and in Figure 9 with respect to the End Of Injection (EOI) of the second injection. As expected, the first pulse results to be independent from the residual magnetization effect on the coils, since all the profiles are almost overlapped. Conversely, synchronizing the curves at the EOI of the second injection pulse, the contribution of the electrical effect can be clearly highlighted. In fact, the lower the DT, the steeper the curve in correspondence of the opening phase, mainly due to the presence of a residual magnetization energy that the electric circuit has not dissipated yet when the second electric pulse is applied.

[Insert Figure 9]

Figure 9: Mean current driving profiles in the injector coils synchronized at EOI_2*.*

Consequently, with respect to the nominal operation, the needle experiences a greater force during the acceleration opening phase, which comes from the contribution of both the residual magnetization energy of the first injection and the second electrical pulse [19]. As a result, the injector coil is able to reach earlier the maximum current, leading the injector needle to experience a greater acceleration during the opening phase with respect to the nominal operation. Since the injector closing phase takes the same time for all the profiles investigated, the current excitation is applied for a longer period thus resulting in a greater fuel mass delivered.

268 Since the deviation of the injected fuel mass with respect to the target value might lead to an increase in fuel consumption, emissions and torque delivered, the following step of the present activity consisted in the development of a predictive model based on electrical considerations aimed at quantifying the deviation between the amount of injected fuel and the target quantity.

272 **RESULTS AND DISCUSSION**

273 In the next sections the methodology aimed at the recognition of the residual magnetization effect relying on the shape of the driving current profiles is presented. Its aim is to compensate the deviation by tuning the ET during the second injection to target the fuel mass to the desired quantity. It is interesting to notice that, in this work, the downstream pressure of the injector is always equal to atmospheric pressure, whereas the injectors installed in engines work with downstream pressures (generally) higher than the atmospheric pressure. This means that the masses injected with the discussed layout might be slightly higher than those measured in different specific engine applications. However, this work identifies a methodological approach suitable to model and compensate the electrical interactions (essentially independent of injector downstream pressure) between close injections, which will remain valid when applied to an in-vehicle installed injector.

283 **i) Equivalent Energizing Time Modelling**

284 The residual magnetization phenomenon impacts on the injected fuel mass as the second injection pulse experiences a quicker opening stage and, consequently, remains open for a longer time. To characterize such influence, an analysis on the variation of the driving current profiles (with respect to the nominal shape) has been conducted. In Figures 10, 11 and 12 the real driving profiles are compared with the same signals in the hypothesis of absence of the electric magnetization effect, providing a visual representation of the phenomenon. To properly acquire the driving current profiles, since the actual current clamp is characterized by a low Signal-to-Noise Ratio (SNR), the inverter that drives the HP pump has been switched off to avoid the signal corruption provided by its magnetic field. Hence, during the tests, no fuel injection has been performed. For each injection pressure value selected, three ETs for both the first and the second pulses have been considered. Firstly, an ET of 400 μs has been selected to study the behaviour of the current profile during the

ballistic operation. Similarly, an ET of 700 μs has been selected for the linear operation. Finally, a third ET between 400 and 700 μs has been selected representing the transitional point from the ballistic to the linear operation ranges. The latter point changes according to the selected injection pressure. Table 4 summarizes the test conditions for the driving current profiles.

Table 4: Tests conditions to characterize the driving current profiles.

ET 1 [μs]	ET 2 [μs]	Injection Pressure [bar]	Dwell Time [μs]
400	400	300	50:50:1500
450	450		
700	700		
400	400	500	
510	510		
700	700		
400	400	700	
600	600		
700	700		

To inject the desired fuel mass, the ET of the second pulse must be reduced in a way which properly compensates the effect of the residual magnetization. At this stage, the amount of the correction of the second ET is unknown and needs to be determined after an investigation of the correlations between the residual magnetization and the fuel mass deviation. To characterize the electrical phenomenon on the coils during the second injection pulse, the difference between the real electric charge and the equivalent one in absence of the phenomenon has been evaluated. The electric charge has been computed as stated in Equation 1.

$$Q = \int_{SOI_1}^{EOI_2} i(t)dt \qquad [C] \tag{1}$$

The equivalent unmagnetized signals (black dashed curves in Figures 10, 11 and 12) have been obtained rigidly translating the current profile of the first injection and imposing the same EOI position for the second injection. Analysing Figure 10, Figure 11 and Figure 12, two main aspects can be highlighted. The first one, as above mentioned, is related to the different value of the derivative during the opening phase, which results in an equivalent greater ET. The second one to mention is the occurrence of a higher Ipeak (with respect to the nominal profile), which results in a stronger force applied to the injector needle. This kind of approach has proved to be able to also detect the reduction of the applied electric charge given by the overlap between the first and the second pulses, as highlighted by the lost triangular green area in Figure 10. Even if its magnitude might be considered negligible, an overall reduced magnetic energy on the coil is generated due to the uncomplete closing at the opening stage and at the lost initial phase at the second pulse.

[Insert Figure 10]

Figure 10: Effect of the residual magnetization on the shape of the current driving profiles applying a low ET at the electrical fusing condition.

[Insert Figure 11]

Figure 11: Effect of the residual magnetization on the shape of the current driving profiles applying a low ET outside the electrical fusing condition.

[Insert Figure 12]

Figure 12: Effect of the residual magnetization on the shape of the current driving profiles applying a high ET outside the electrical fusing condition.

As stated by Equation 1, computing the electric charge to each current driving profile, Figure 13 shows the effect of the residual magnetization phenomenon on the amount of electric charge in relation to the imposed DT. In particular, the shape of the blue curve (denoted as "A1: Magnetized") is directly related to the greater derivative and Ipeak of the real current profile. In fact, while the DT is increased, the real electric charge tends to drop until it reaches its nominal value, which is represented by the dashed black curve ("A2: Equivalent unmagnetized"). The effect of the current overlap is evidenced by the first points of the black curve, which shows that the equivalent unmagnetized electric charge starts from a lower value with respect to the steady one. To compute both the effects of the magnetization phenomenon and the electric charge reduction due to the current overlap, the difference between the magnetized (A1) and equivalent unmagnetized (A2) curves has been calculated, resulting in the dotted red curve (A3: A1-A2).

[Insert Figure 13]

Figure 13: Electric charge on the injector coil with respect to DT adopting a low ET at low injection pressure.

[Insert Figure 14]

Figure 14: Electric charge on the injector coil with respect to DT adopting a high ET at high injection pressure.

As expected, in both cases shown in Figure 13 and Figure 14, the difference of the profiles tends to zero while the DT increases.

In order to relate the amount of the electric charge on the coil with the equivalent ET (ET_{eq}) applied to the injector, a relation based on the trends reported in Figure 13 and Figure 14 has been proposed. In particular, the difference between the magnetized and equivalent unmagnetized curves has been evaluated (also considering the current overlap effect). It yields:

$$ET_{eq} = \left[\frac{A_3(DT)}{\max\left(A_3(DT)\right)} + 1\right] * ET_1 \qquad [\mu s] \tag{2}$$

The above equation directly relates the percentage increase of the difference between the profiles ($\frac{A_3}{\max(A_3)}$) with the ET_1, which is the one imposed during the first pulse. Figure 15 reports, with respect to the DT between the injections, the ET_{eq} obtained applying Equation 2 to each tested condition with a nominal ET of 400 μs.

[Insert Figure 15]

Figure 15: Behaviour of ET_{eq} with respect to the DT for all the injection pressure conditions with a ET_1 of 400 μs (a) and ET_1 of 700 μs (b).

[Insert Figure 16]

Figure 16: Behaviour of ET_{eq} with respect to the DT for an injection pressure of 500 bar varying the ET_1.

Figure 15a and Figure 15b are obtained using ET_1 equal to 400 and 700 μs, respectively. Comparing those curves, no significant impact on the Ipeak can be noticed if the ET_1 is kept the same. On the other hand, Figure 16 highlights a strong dependence of the actual value of ET_1, In fact, the shape of the ET_{eq} curve rigidly scales to greater values as ET_1 increases. The latter result is due to the higher residual magnetization energy supplied by ET_1 during the first pulse. Hence, the residual magnetization phenomenon is clearly independent from the actual Ipeak, which depends on the operative injection pressure.

[Insert Figure 17]

Figure 17: Comparison of ET_{eq} in three different peak current conditions.

As a matter of fact, Figure 17 highlights that the surfaces of ET_{eq} with respect to the variation of both DT and ET_1 are independent from the different Ipeak conditions. The latter consideration allows the adoption of just one single surface for the determination of the ET_{eq}, which depends only on the ET of the first injection and on the Dwell Time between the two events.

In order to validate the proposed model, a predicted mass has been estimated interpolating the injector map with rail pressure and ET_{eq}, which has been obtained directly from the map of Figure 17 using the ET_1 and the

DT. Then, the predicted mass from the model has been compared with the experimental one in the same conditions. A graphical explanation of the procedure is shown in Figure 18.

[Insert Figure 18]

Figure 18: Procedure for the model validation.

ii) Compensation of the residual magnetization effect

Adopting the procedure reported in Figure 18, it is possible to estimate the total injected mass. Figures 19, 20 and 21 show a comparison between the results of the model and the real experimental data for each injection pressure investigated. In particular, the red dashed-dotted line represents the percentage error between experiments and model. The characterization of the residual magnetization phenomenon using the increase of electric charge of the current driving profiles allows to keep the error in a range of almost $\pm 5\%$ in most of the DT investigated.

[Insert Figure 19]

Figure 19: Comparison between estimated and experimental injected mass for 300 bar of injection pressure and $ET_1 = 700\ \mu s$.

[Insert Figure 20]

Figure 20: Comparison between estimated and experimental injected mass for 500 bar of injection pressure and $ET_1 = 700\ \mu s$.

[Insert Figure 21]

Figure 21: Comparison between estimated and experimental injected mass for 700 bar of injection pressure and $ET_1 = 700\ \mu s$.

The model has been able to accurately reproduce the injector behaviour in terms of injected mass during multiple pulses in a wide range of DT. During the transition between the hydraulic overlapping and the separated injections phases, the model deviates from the experiments and the error becomes around 10% for all the three injection pressures considered. However, the deviation of the model occurs in a range of DT which are practically unused, since the hydraulic fusing phase depends only on the dynamics inside the injector itself, which cannot be controlled or avoided, and is usually excluded by the selected operating conditions. For this reason, the relation of Equation 2 can be considered valid in the hypothesis of completely separated injections, for which both the electric and hydraulic overlap operations don't occur.

Since the objective of the present paper is to target the actual injected mass to the desired quantity, the discussed model has been inverted to properly correct the ET of the second pulse and compensate the effect of the residual magnetization phenomenon. In particular, the map in Figure 17 has been elaborated in MATLAB using the *cftool* algorithm to obtain the coefficients of a polynomial equation in terms of DT and ET. Considering the shape of the surface in Figure 17, a linear dependence on ET and a cubic dependence on DT have been adopted, as reported in Equation 3. Further details regarding the coefficients of Equation 3 can be found in Appendix A.

$$ET_{eq} = f(DT^3, ET_1) = a_{00} + DT(a_{10} + a_{20}DT + a_{30}DT^2) + ET_1(a_{01} + a_{11}DT + a_{21}DT^2) \qquad [\mu s] \qquad (3)$$

The fitted surface related to the determination of ET_{eq} is shown in Figure 22a. Based on this calibrated surface, the corrected ET necessary to inject the target fuel mass can be finally determined. Under the assumption of imposing for both the pulses the same ET, it has to be taken into account that at the second ET has to be added a ΔET, due to the magnetization energy effect, determining an equivalent ET evaluated by the following Equation 4:

$$ET_{eq} = ET_2 + \Delta ET(ET_1, DT) \qquad [\mu s] \qquad (4)$$

Hence, in order to inject the required fuel, the resultant ET_{eq} must be the same of the one applied during the first pulse ($ET_{eq} = ET_1$). In other words, the ET_2 must be reduced of a quantity equal to ΔET to provide the correct amount of fuel injected. Equation 5 gives a mathematical representation of the concept.

$$ET_2 = ET_1 - \Delta ET(ET_1, DT) \qquad [\mu s] \qquad (5)$$

A graphical interpretation of the procedure is shown in Figure 22b, where the blue curve represents the intersection between the fitted surface and the plane at 500 μs (for example). As shown in figure 22a, the slope of this curve directly depends on the actual value of DT: the higher the DT, the lower the slope, since it is directly related to the residual magnetization effect. If the ET of the second pulse is set equal to ET_1, the magnetization phenomenon induces an injected mass increase due to the longer equivalent ET as shown in Figure 22b looking at point A. Thus, to inject the required fuel mass and counterbalance the magnetization effect, an $ET_{corrected}$ must be imposed to allow $ET_{eq} = ET_1$. In this way, even if the magnetization phenomenon is still present, the reduction of the ET2 during the second injection would be able to target the injected fuel to the desired quantity (point B in Figure 22b).

[Insert Figure 22]

Figure 22: (a) Fitted surface for ET_{eq} and intersection with the red plane at DT=500 μs;
(b) Explanation of the increased ET if $ET_1 = ET_2$ (point A) and determination of the corrected ET (point B).

Repeating the same procedure for each value of ET_1 and DT, the inverted map of Figure 23 has been obtained. For the lowest values of ET_1, an extrapolation procedure has been beneficial to calculate the $ET_{corrected}$.

[Insert Figure 23]

Figure 23: Map for the corrected ET.

Consequently, the map shown in Figure 23 has been used to evaluate the $ET_{corrected}$ to inject the desired fuel mass compensating the effect of the residual magnetization. For all the injection pressures investigated, the $ET_{corrected}$ of the second pulse have been determined in function of ET_1 and DT for each test. Table 5 summarizes the information related to the tests aimed at the validation.

Table 5: Tests conditions for the validation procedure.

ET 1 [μs]	ET 2 [μs]	Injection Pressure [bar]	Dwell Time [μs]
700	$f(ET_1, DT)$	500	300:50:1500
		300	400:50:950
		700	350:50:950

The first tests for the validation involve an intermediate injection pressure of 500 bar and the complete range of DT from the hydraulic overlap operation to 1500 μs, value at which the magnetization effect should be negligible. Figure 24 compares the injected fuel mass in both the not corrected and corrected conditions with respect to the reference value, that corresponds to the value at which the injected fuel tends once the magnetization phenomenon disappears (dotted grey horizontal line). Similarly, Figure 25 highlights the percentage error with respect to the reference value for the same conditions. As showed by both Figures 24 and 25, applying the corrections determined with the inverted map, the injected fuel mass lies around the reference value, owing to a reduced error. Moreover, the correction provided by the model could be considered negligible for DT greater than 1000 μs since, as depicted in Figure 25, the error with respect to the reference value is almost the same for both the not corrected and corrected curves. Consequently, during the tests involving different injection pressures, the maximum value of DT has been fixed at 950 μs.

The results related to the validation of the model for two injection pressures of 300 and 700 bar are plotted in Figures 26 and 27, respectively. Analysing the not-corrected curves for all the injection pressure conditions, it is clear that a higher injection pressure leads to larger errors between the injected and the target quantity (here, the maximum deviation between measured and target injected quantity might reach values close to 25-30%). This is related to the greater Ipeak of the driving profiles, which must be increased to enhance the needle-opening phase according to the actual injection pressure.

[Insert Figure 24]

Figure 24: Comparison between not corrected and corrected fuel injected mass with 500 bar injection pressure and $ET_1 = 700\ \mu s$.

[Insert Figure 25]

Figure 25: Comparison between the error of not corrected and corrected fuel injected mass with 500 bar injection pressure and $ET_1 = 700\ \mu s$.

For all the injection pressures analyzed, the correction on the ET of the second pulse allows a significant reduction of the error, which lies in the range of $\pm$ 5 %. On the other hand, the shape of injected masses and errors (not corrected and corrected curves) suggests that the fuel mass deviation from the target value might also depend on other factors.

[Insert Figure 26]

Figure 26: (a) Comparison between not corrected and corrected fuel injected mass with 300 bar injection pressure and $ET_1 = 700\ \mu s$; (b) Comparison between the error of not corrected and corrected fuel injected mass with 300 bar injection pressure and $ET_1 = 700\ \mu s$.

[Insert Figure 27]

Figure 27: (a) Comparison between not corrected and corrected fuel injected mass with 700 bar injection pressure and $ET_1 = 700\ \mu s$; (b) Comparison between the error of not corrected and corrected fuel injected mass with 700 bar injection pressure and $ET_1 = 700\ \mu s$.

As a matter of fact, corrected and not corrected curves present peaks and valleys, advising that other phenomena are involved in this characterization. A preliminary analysis suggests that the residual errors are mainly due to the effects of pressure waves propagation in the feed ducts of the injectors. This effect in not taken into account in the proposed methodology, and it will be better examined in future works.

CONCLUSIONS AND FUTURE WORK

The current paper analyses the performance of an ultra-high injection pressure GDI injector, with a particular focus on the behaviour during closely spaced injection strategies, which are implemented in most LTC systems. First, the hydraulic characterization of the injector has been carried out thanks to the development of a dedicated hydraulic test bench. The preliminary results showed that the transition between the ballistic and linear operation range increases according to the actual injection pressure. To overcome the uncertainties related to the low repeatability of the injected mass, an ET of 700 μs has been selected to allow the fuel to operate always in the linear region for all the injection pressures investigated (300, 500 and 700 bar).

To understand the behaviour of the injected mass, experimental tests have been conducted by progressively increasing the DT between the two injections from 50 up to 4000 μs. Results provided that the fuel injected mass is influenced by the DT between the first and the second pulse: the more the injections are close, the higher is the overall injected mass respect to the target value. The latter phenomenon is attributed to the residual

478 magnetization energy in the injector coils once the second pulse is imposed, inducing a greater electric charge
479 affecting the needle dynamic behaviour.

480 The residual magnetization phenomenon has been modelled directly analysing the current driving profiles. The
481 deviation of the profiles from the nominal shape resulted to be independent from the value of the peak current,
482 while it is strongly influenced by the DT between the two injections. Therefore, a correlation has been derived
483 which relates the increase of electric charge with respect to the nominal operation and an equivalent ET. To
484 validate the latter correlation, the experimental injected mass has been compared with the same given by the
485 interpolation of the injector map adopting the actual injection pressure and the modelled equivalent ET. Apart
486 from the hydraulic overlapping phase, which is not of interest, the model allows to efficiently fit the
487 experiments providing an error always in the range of ± 5 % for each injection pressure and DT investigated.

488 Once the model has been validated, it has been inverted to address the fuel injected mass to the desired quantity.
489 As a result, the correction of the ET during the second pulse, derived from the inverted model, allows the fuel
490 injected mass to lie in the range of ± 5 % with respect to the target quantity. Future studies will regard the
491 complete characterization of the injection system behavior, with the aim to develop a control strategy able to
492 compensate both electrical and hydraulic phenomena effects on the injected mass.

493 **UNCERTAINTIES**

494 This section describes the information about the most important sensors used by the authors during the
495 presented study.

496 - Pressure wave propagation inside the injector pipes.

Element	Value
Sensor name	Kistler 4067A
Measuring range	0-2000 bar
Overload	500 bar
Sensitivity	5 mV/bar
Linearity	≤± 0.5
Natural frequency	> 100 kHz

497

498 - Fuel Injected mass.

Element	Value

Sensor name	AVL Balance 733s
Measuring range	0-150 kg/h
Measurement uncertainty	$\leq\pm$ 0.12 %
Maximum measurement frequency	10 Hz

- Driving current profiles.

Element	**Value**
Sensor name	Hioki CT6846A
Rated current	1000 A AC/DC
Frequency bandwidth	DC – 100 kHz
Max allowable input	$\pm$ 1900 Apeak
Accuracy	DC: 0.2 % + 0.02% DC < f < 100 kHz: 0.2% + 0.01%
Linearity	$\pm$ 20 ppm

APPENDIX A

The current section reports the coefficients computed by the *cftool* toolbox in MATLAB to fit the surface for the ET_{eq} evaluation (Equation 3).

a_{30}	a_{20}	a_{10}	a_{21}	a_{11}	a_{01}	a_{00}
$-5.2 * 10^{-7}$	$1.3 * 10^{-3}$	-0.95	$4.8 * 10^{-7}$	$-1.2 * 10^{-3}$	1.74	165.2

REFERENCES

[1] Zhao, F., Lai, M. C., & Harrington, D. L. (1999). Automotive spark-ignited direct-injection gasoline engines. *Progress in Energy and Combustion Science*, *25*(5). https://doi.org/10.1016/S0360-1285(99)00004-0.

[2] Catapano, F., di Iorio, S., Magno, A., & Vaglieco, B. M. (2022). Effect of fuel quality on combustion evolution and particle emissions from PFI and GDI engines fueled with gasoline, ethanol and blend, with focus on 10–23 nm particles. *Energy*, *239*. https://doi.org/10.1016/j.energy.2021.122198.

[3] Saliba, G., Saleh, R., Zhao, Y., Presto, A. A., Lambe, A. T., Frodin, B., Sardar, S., Maldonado, H., Maddox, C., May, A. A., Drozd, G. T., Goldstein, A. H., Russell, L. M., Hagen, F., & Robinson, A. L. (2017). Comparison of Gasoline Direct-Injection (GDI) and Port Fuel Injection (PFI) Vehicle Emissions: Emission Certification Standards, Cold-Start, Secondary Organic Aerosol Formation Potential, and Potential Climate Impacts. *Environmental Science and Technology*, *51*(11), 6542–6552. https://doi.org/10.1021/acs.est.6b06509.

[4] Chen, L., Liang, Z., Zhang, X., & Shuai, S. (2017). Characterizing particulate matter emissions from GDI and PFI vehicles under transient and cold start conditions. *Fuel*, *189*, 131–140. https://doi.org/10.1016/j.fuel.2016.10.055.

[5] Dahlander, P., Babayev, R., Ravi Kumar, S., Etikyala, S. et al., "Particulates in a GDI Engine and Their Relation to Wall-Film and Mixing Quality," SAE Technical Paper 2022-01-0430, 2022, https://doi.org/10.4271/2022-01-0430.

[6] Mamakos, A., Steininger, N., Martini, G., Dilara, P., & Drossinos, Y. (2013). Cost effectiveness of particulate filter installation on Direct Injection Gasoline vehicles. Atmospheric Environment, 77. https://doi.org/10.1016/j.atmosenv.2013.04.063.

[7] Lou, D., Wang, T., Fang, L., Tan, P., Hu, Z., Zhang, Y., Xu, Z., Cheng, C., Wang, S., & Zhang, Y. J. (2022). Investigation of the combustion and particle emission characteristics of a GDI engine with a 50 MPa injection system. *Fuel*, *315*. https://doi.org/10.1016/j.fuel.2021.123079.

[8] Befrui, B., Hoffmann, G., Spiekermann, P., Piock, W.F. (2017). A Comparative Study of the Fuel Pressure and Temperature Effects on the GDi Multi-Hole Spray. In: Tschöke, H., Marohn, R. (eds) 10. Tagung Diesel- und Benzindirekteinspritzung 2016. Proceedings. Springer Vieweg, Wiesbaden. https://doi.org/10.1007/978-3-658-15327-4_15.

[9] Y. Yu. Experimental study on effects of ethanol-diesel fuel blended on spray characteristics under ultra-high injection 452 pressure up to 350 MPa. Energy. 186 (2019) 115768. https://doi.org/10.1016/j.energy.2019.07.098.

[10] Zheng, Z., Tian, X., & Zhang, X. (2015). Effects of split injection proportion and the second injection time on the mixture formation in a GDI engine under catalyst heating mode using stratified charge strategy. *Applied Thermal Engineering*, *84*. https://doi.org/10.1016/j.applthermaleng.2015.03.041.

[11] Muddapur, A., Sahu, Dr. S., Jose, J. v., & Sundararajan, T. (2022). Spray-Wall Impingement in a Multi-Hole Gdi Injector for Split Injection at Elevated Wall Temperature and Ambient Conditions. *SSRN Electronic Journal*. https://doi.org/10.2139/ssrn.4000406.

[12] Lee, Z., Kim, T., Park, S., & Park, S. (2020). Review on spray, combustion, and emission characteristics of recent developed direct-injection spark ignition (DISI) engine system with multi-hole type injector. In *Fuel* (Vol. 259). https://doi.org/10.1016/j.fuel.2019.116209.

[13] Krishnamoorthi, M., Malayalamurthi, R., He, Z., & Kandasamy, S. (2019). A review on low temperature combustion engines: Performance, combustion and emission characteristics. In *Renewable and Sustainable Energy Reviews* (Vol. 116). https://doi.org/10.1016/j.rser.2019.109404.

[14] Zhou, L., Dong, K., Hua, J., Wei, H., Chen, R., & Han, Y. (2018). Effects of applying EGR with split injection strategy on combustion performance and knock resistance in a spark assisted compression ignition (SACI) engine. *Applied Thermal Engineering*, *145*. https://doi.org/10.1016/j.applthermaleng.2018.09.001.

[15] Cho, K., Zhao, L., Ameen, M., Zhang, Y. et al. (2019). Understanding Fuel Stratification Effects on Partially Premixed Compression Ignition (PPCI) Combustion and Emissions Behaviors. *SAE Technical Papers,* 2019. https://doi.org/10.4271/2019-01-1145.

[16] Liu L., Zhang Z. ,Liang Y., Zhang F. and Yang B. (2021). Combustion stability control of gasoline compression ignition (GCI) under low-load conditions: A review. In *Applied Mathematics and Nonlinear Sciences*, Vol.6 (Issue 2), pp. 427-446. https://doi.org/10.2478/amns.2021.1.00039.

[17] Ravaglioli, V., Ponti, F., Silvagni, G., Moro, D., Stola, F., & de Cesare, M. (2022). Performance Assessment of Gasoline PPC in a Light-Duty CI Engine. *SAE Technical Papers*, *2022*. https://doi.org/10.4271/2022-01-0456.

[18] Catania, A. E., Ferrari, A., Manno, M., and Spessa, E. (March 28, 2008). Experimental Investigation of Dynamics Effects on Multiple-Injection Common Rail System Performance. *ASME. J. Eng. Gas Turbines Power*. May 2008; 130(3): 032806. https://doi.org/10.1115/1.2835353.

[19] Bai, Y., Gu, Y., Lan, Q., Fan, Y. et al., "Correction Strategy of Fuel Injection Quantity During Pilot-Main Injection of Common Rail System," *Journal of Mechanical Science and Technology* 34, no. 6 (2020): 2647-2656, https://doi.org/10.1007/s12206-020-0538-0.

[20] Cavicchi, A., Postrioti, L., & Scarponi, E. (2019). Hydraulic analysis of a GDI injector operation with close multi-injection strategies. *Fuel*, *235*. https://doi.org/10.1016/j.fuel.2018.08.089.

[21] Silvagni, G., Ravaglioli, V., Ponti, F., Corti, E., Raggini, L., Scocozza, G., Stola, F., & de Cesare, M. (2021). Development of a Predictive Pressure Waves Model for High-Pressure Common Rail Injection Systems. *SAE International Journal of Engines*, *15*(5). https://doi.org/10.4271/03-15-05-0039.

[22] Shannon, C. E. (1949). Communication in the Presence of Noise. *Proceedings of the IRE*, 37(1), 10–21. https://doi.org/10.1109/jrproc.1949.232969.

[23] Moon, S., Atac, O. F., Bae, G., & Park, J. (2023). Comprehensive investigation on ballistic injection characteristics of GDI injector: A particular focus on injection pressure and fuel effects. *Fuel*, 335, 127039. https://doi.org/10.1016/j.fuel.2022.127039.

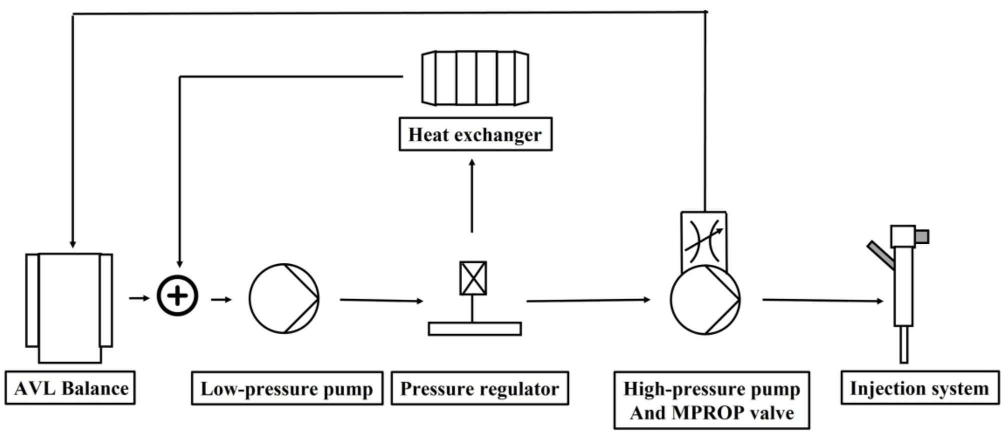

Figure 1: Schematic of the flushing bench system.

316x135mm (300 x 300 DPI)

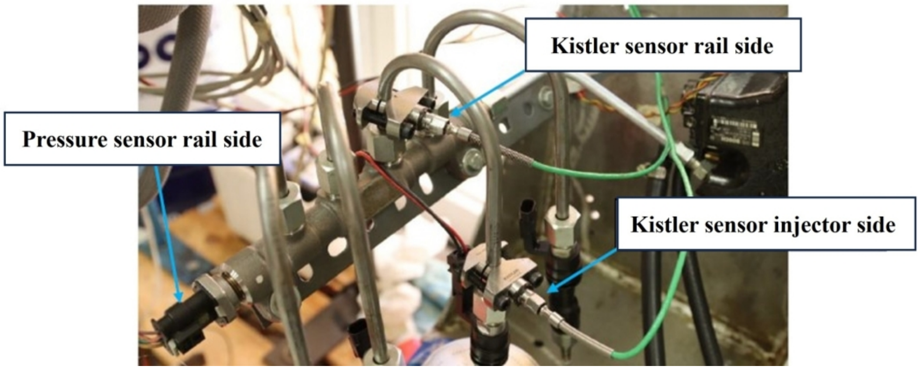

Figure 2: Sensors on the HP system. In particular, the two Kistler sensors have been located at the beginning and at the end of the HP duct between the rail and the injector.

196x83mm (300 x 300 DPI)

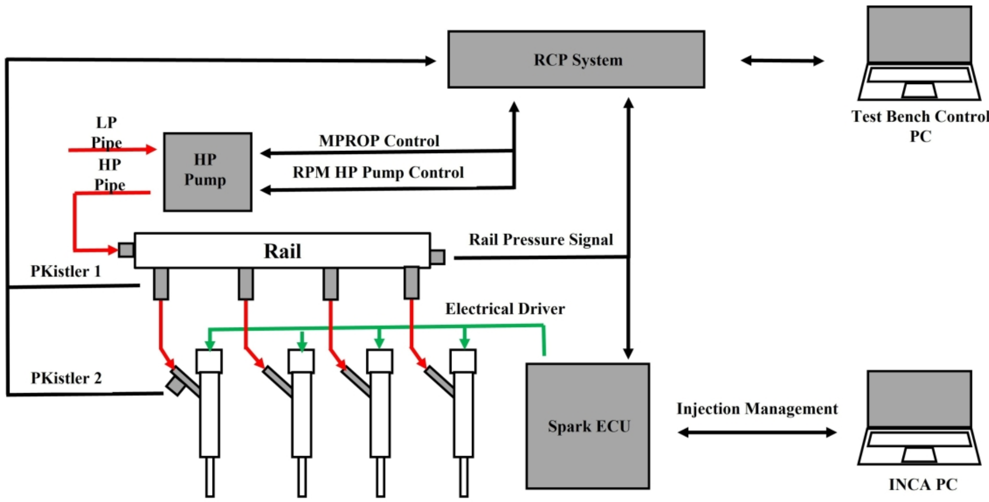

Figure 3: Scheme of flushing bench acquisition and control.

295x147mm (300 x 300 DPI)

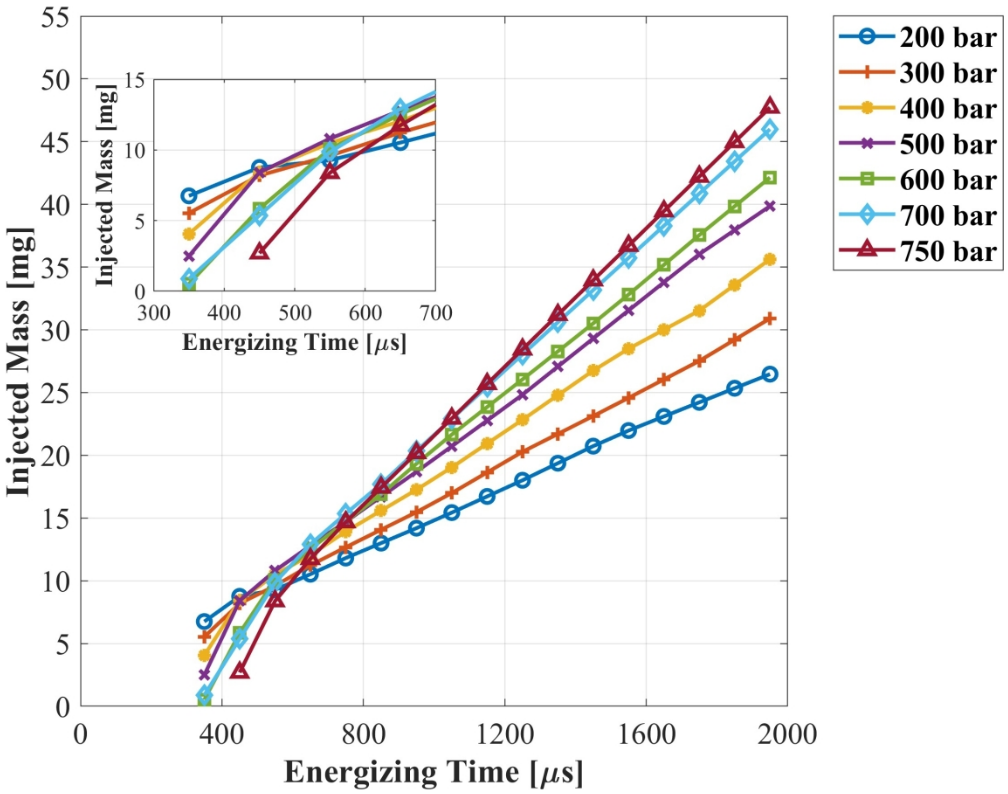

Figure 4: Injected mass with respect to the ET at different injection pressures.

781x612mm (72 x 72 DPI)

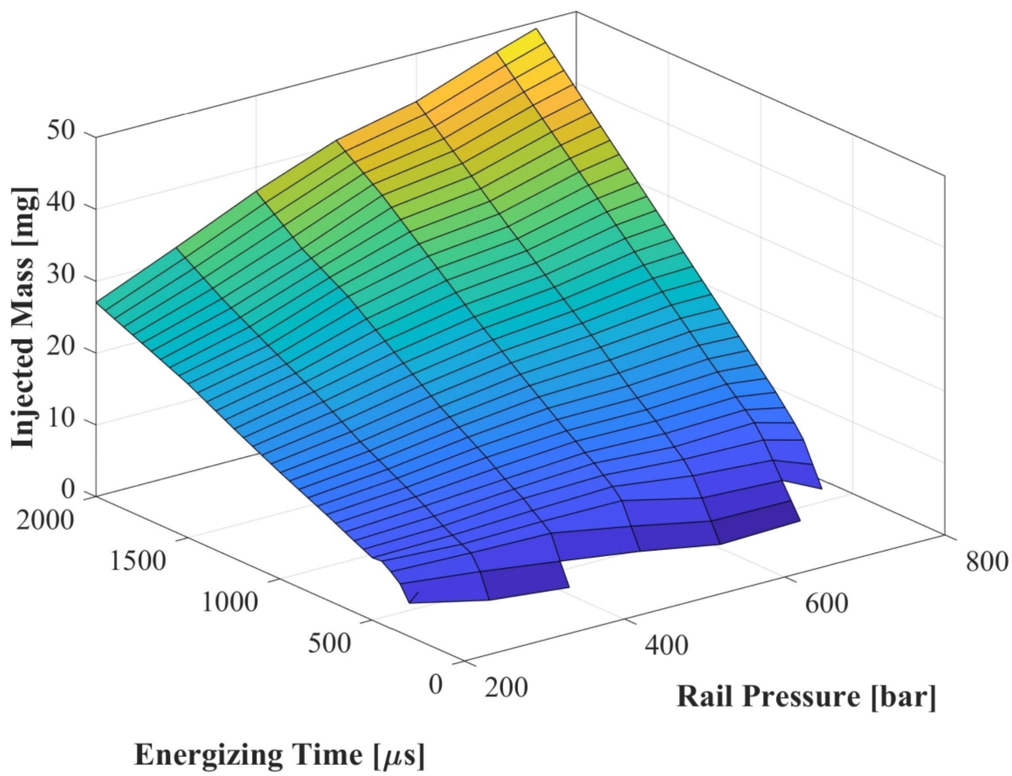

Figure 5: Single pulse injector map.

805x613mm (72 x 72 DPI)

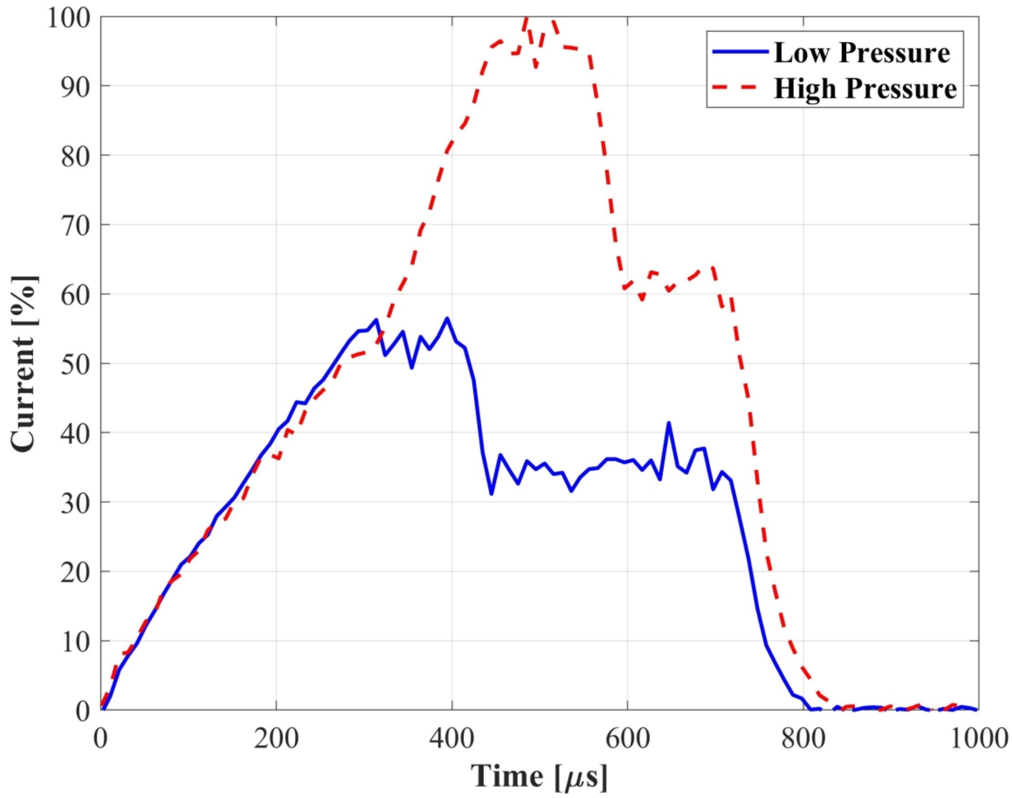

Figure 6: Variation of the current driving profiles shape at different injection pressure and equal ET.

778x613mm (72 x 72 DPI)

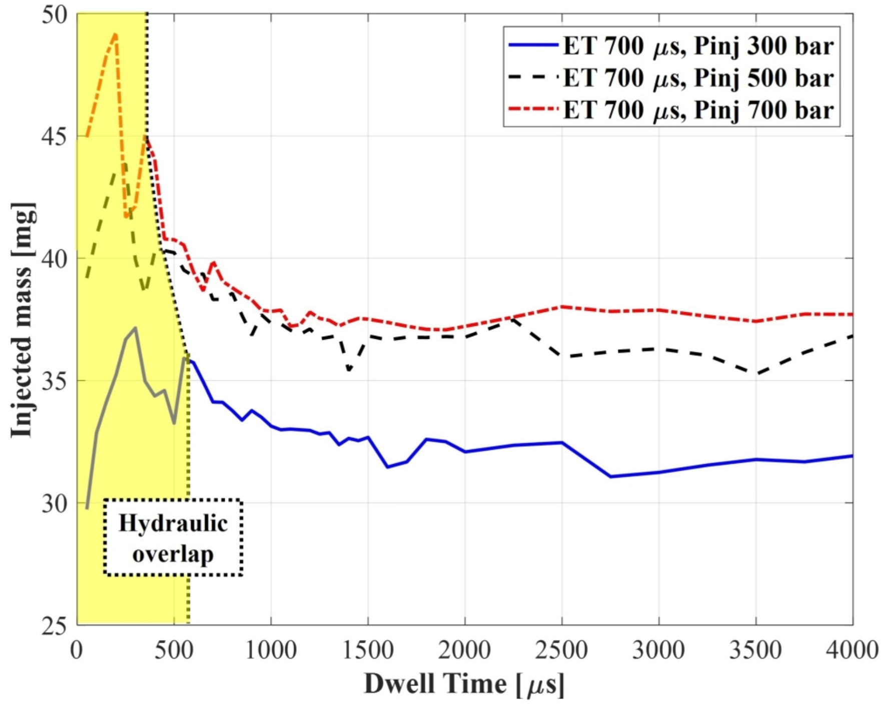

Figure 7: Injected mass variation as a function of the DT between two consecutive injections with ET = 700 μs.

194x145mm (300 x 300 DPI)

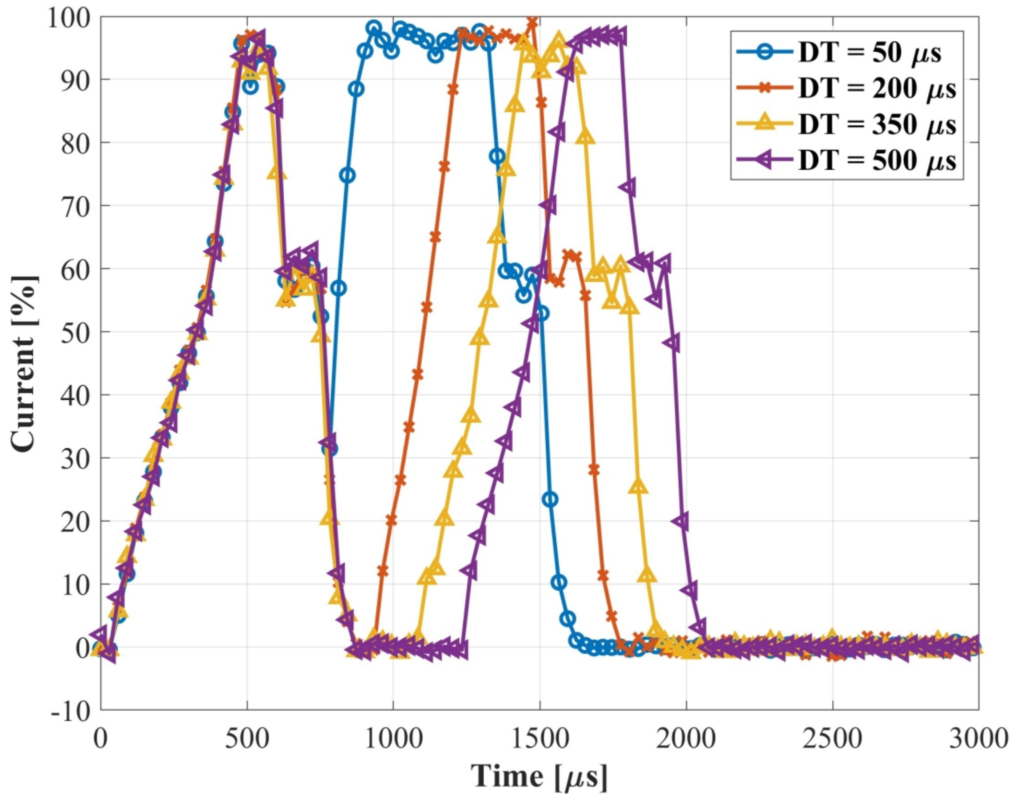

Figure 8: Mean current driving profiles in the injector coils synchronized at SOI_1.

778x613mm (72 x 72 DPI)

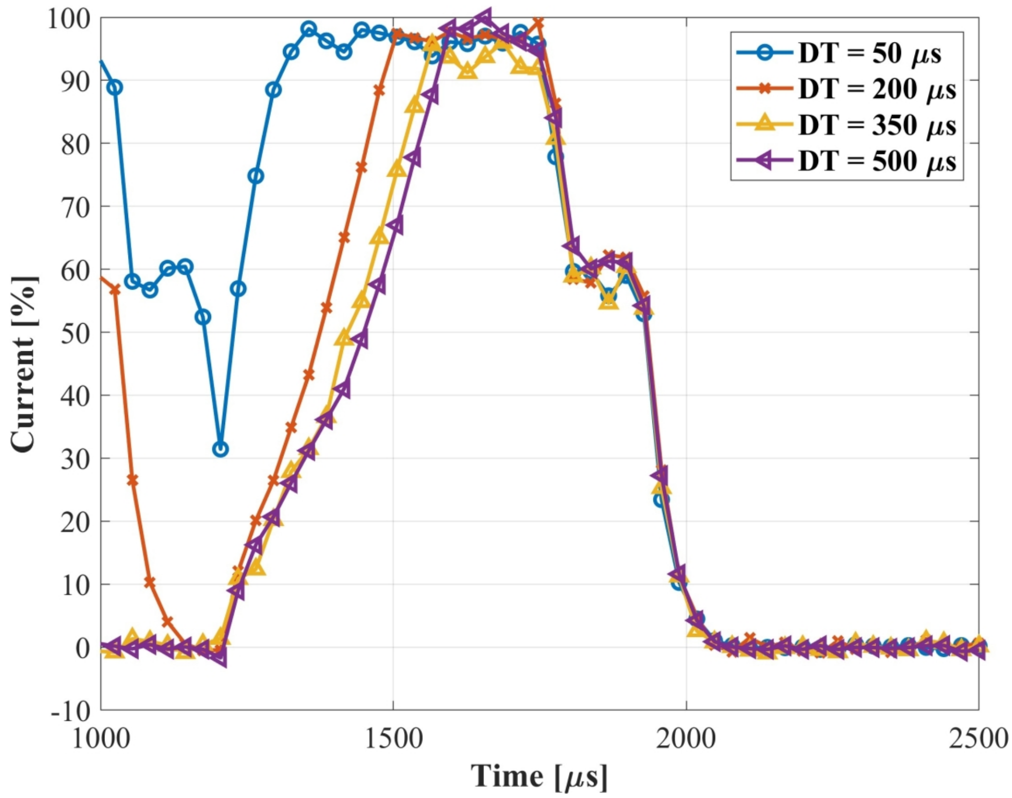

Figure 9: Mean current driving profiles in the injector coils synchronized at EOI_2.

778x613mm (72 x 72 DPI)

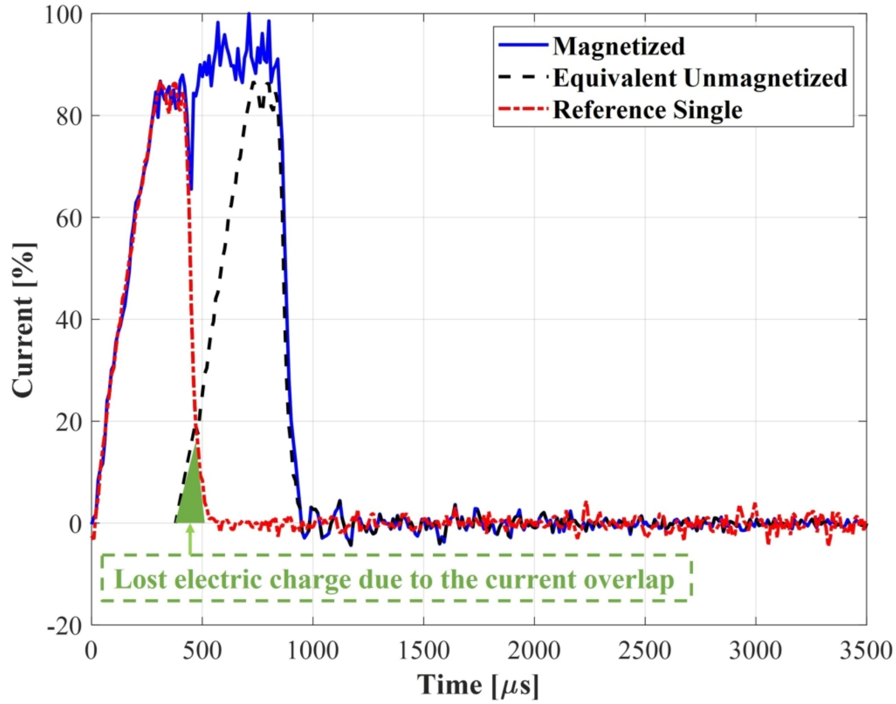

Figure 10: Effect of the residual magnetization on the shape of the current driving profiles applying a low ET at the electrical fusing condition.

223x167mm (300 x 300 DPI)

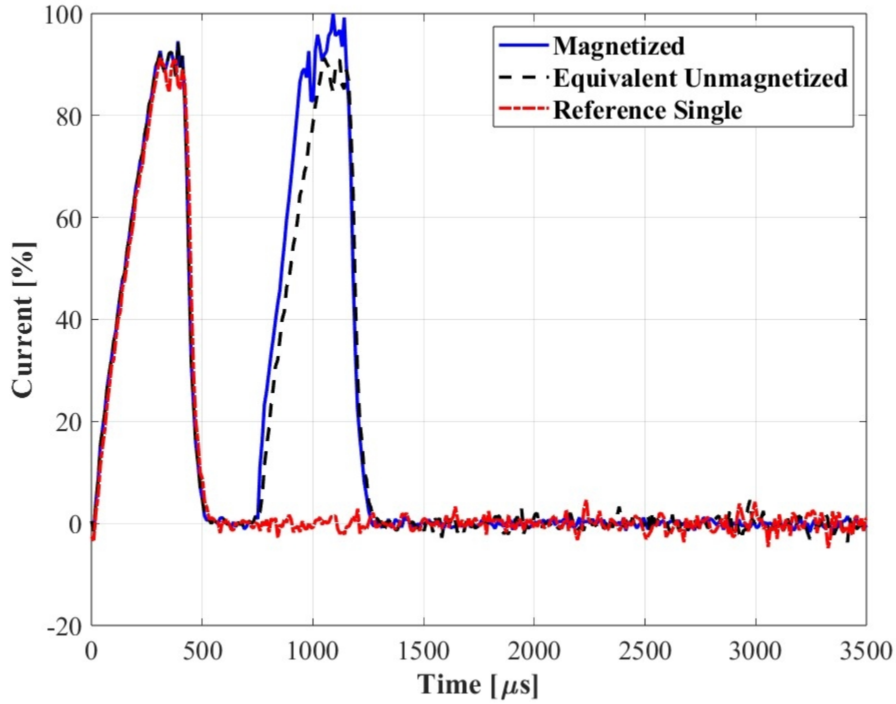

Figure 11: Effect of the residual magnetization on the shape of the current driving profiles applying a low ET outside the electrical fusing condition.

352x264mm (72 x 72 DPI)

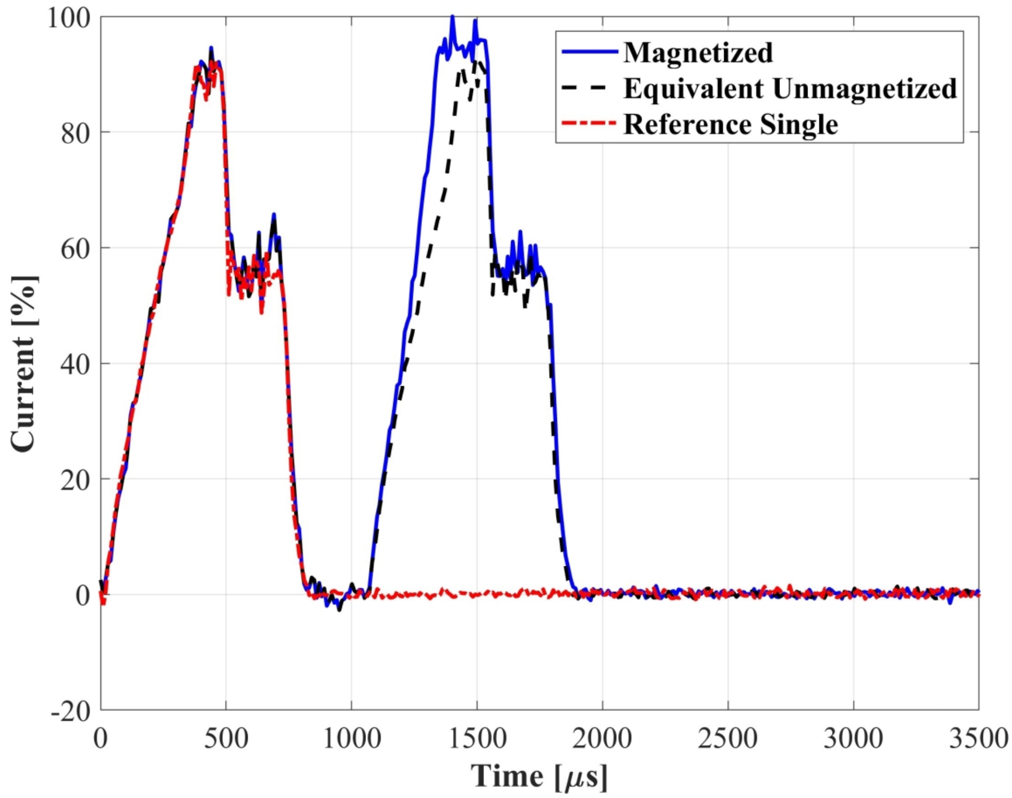

Figure 12: Effect of the residual magnetization on the shape of the current driving profiles applying a high ET outside the electrical fusing condition.

778x613mm (72 x 72 DPI)

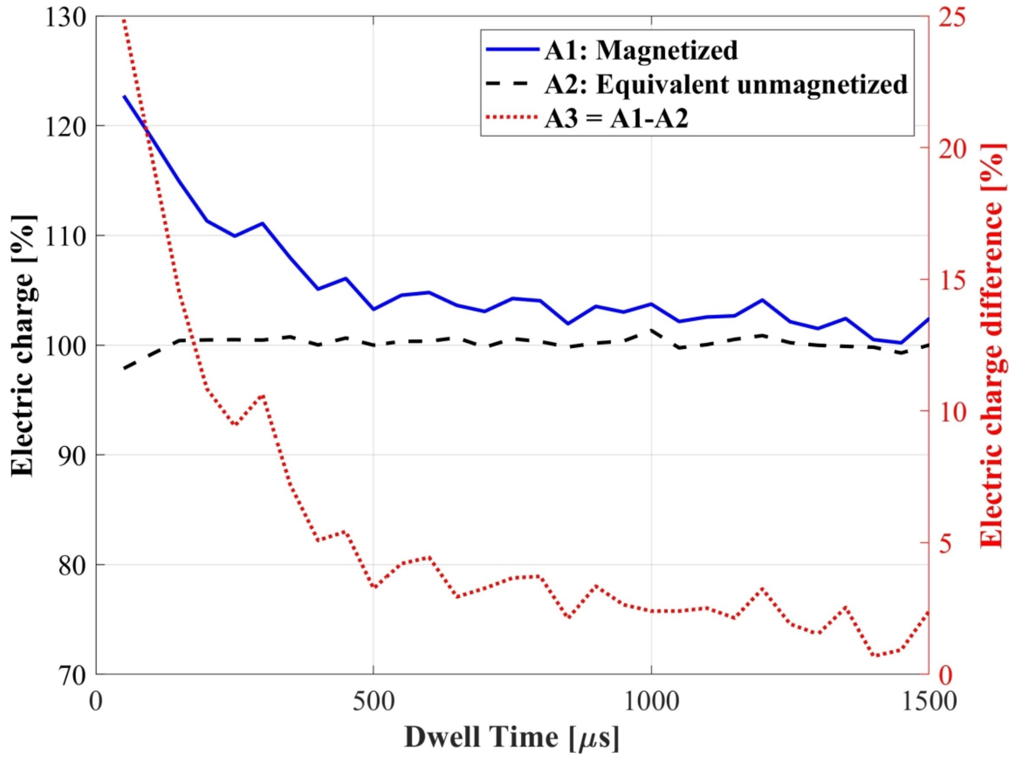

Figure 13: Electric charge on the injector coil with respect to DT adopting a low ET at low injection pressure.

820x613mm (72 x 72 DPI)

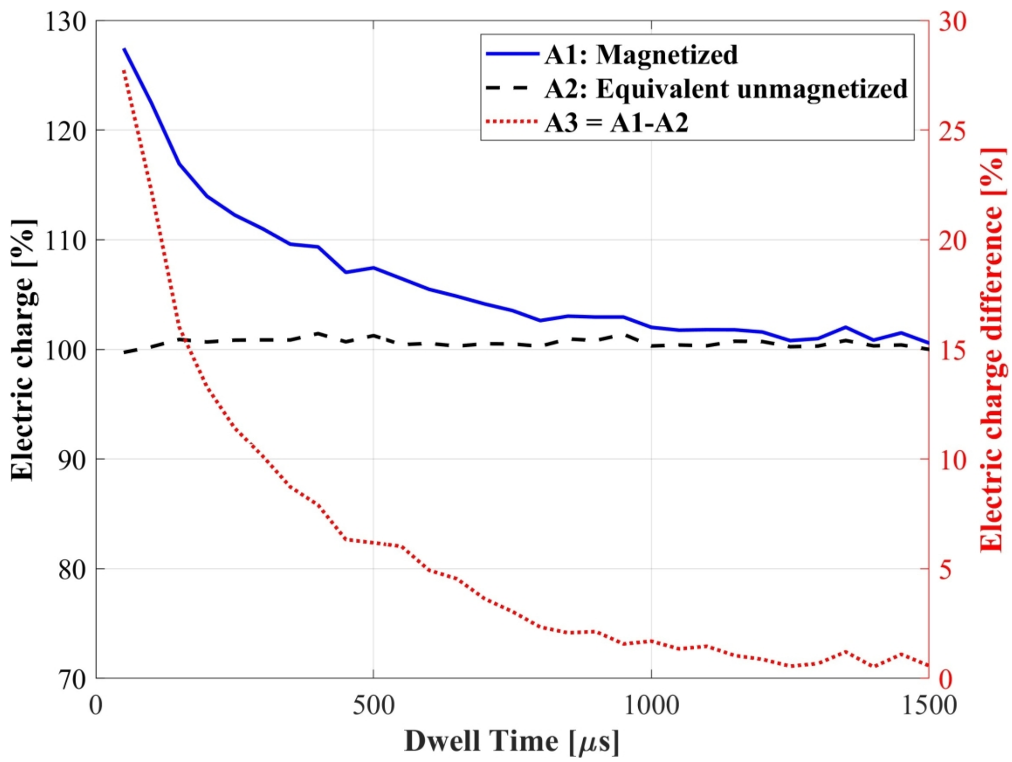

Figure 14: Electric charge on the injector coil with respect to DT adopting a high ET at high injection pressure.

820x613mm (72 x 72 DPI)

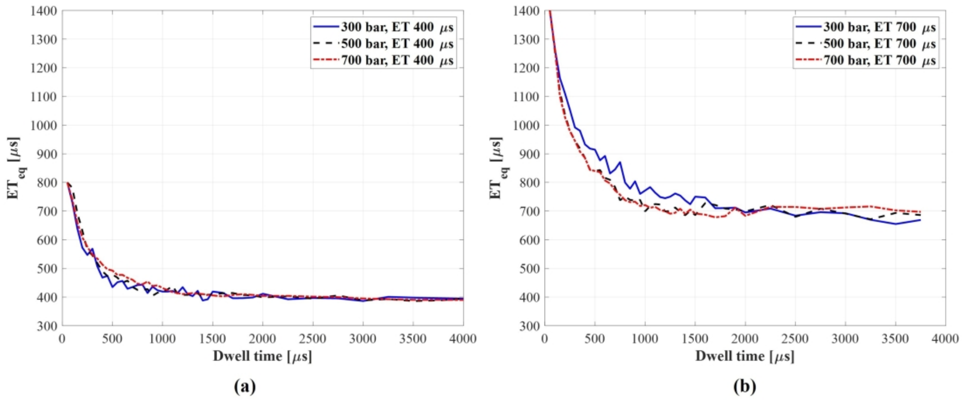

Figure 15: Behaviour of ET_eq with respect to the DT for all the injection pressure conditions with a ET_1 of 400 μs (a) and ET_1 of 700 μs (b).

258x110mm (300 x 300 DPI)

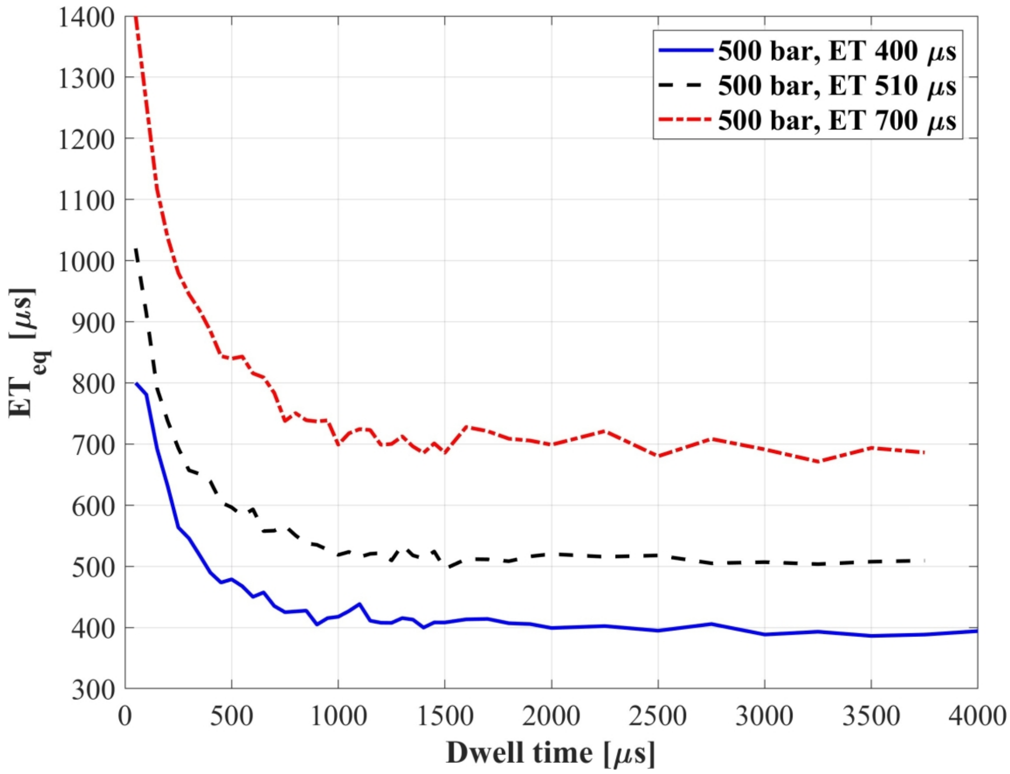

Figure 16: Behaviour of ET_eq with respect to the DT for an injection pressure of 500 bar varying the ET_1.

801x613mm (72 x 72 DPI)

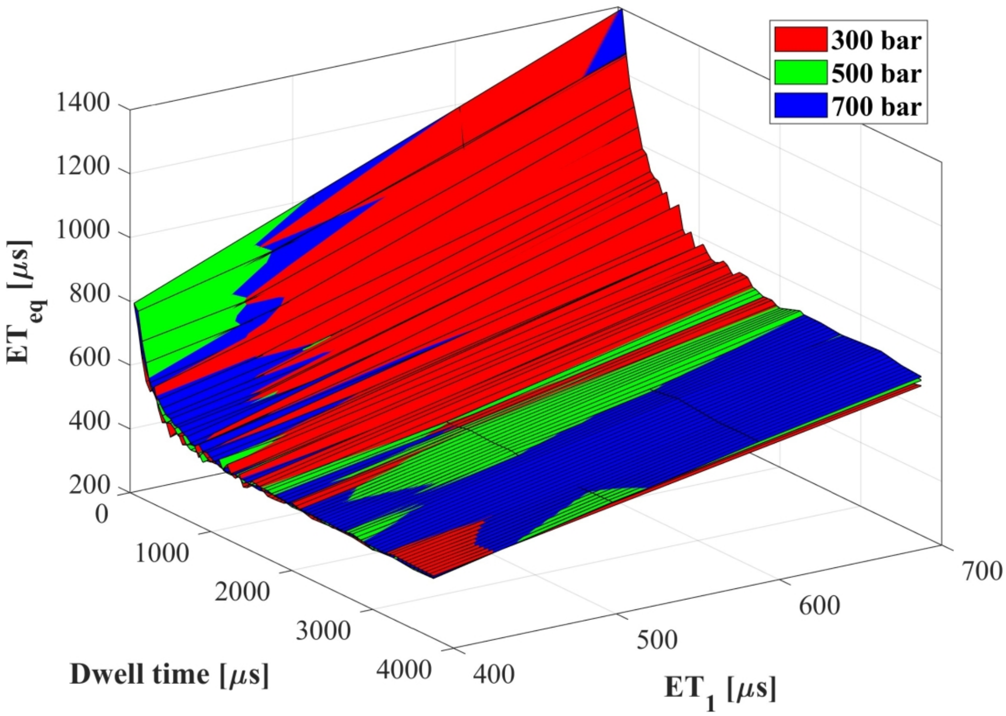

Figure 17: Comparison of ET_eq in three different peak current conditions.

840x594mm (72 x 72 DPI)

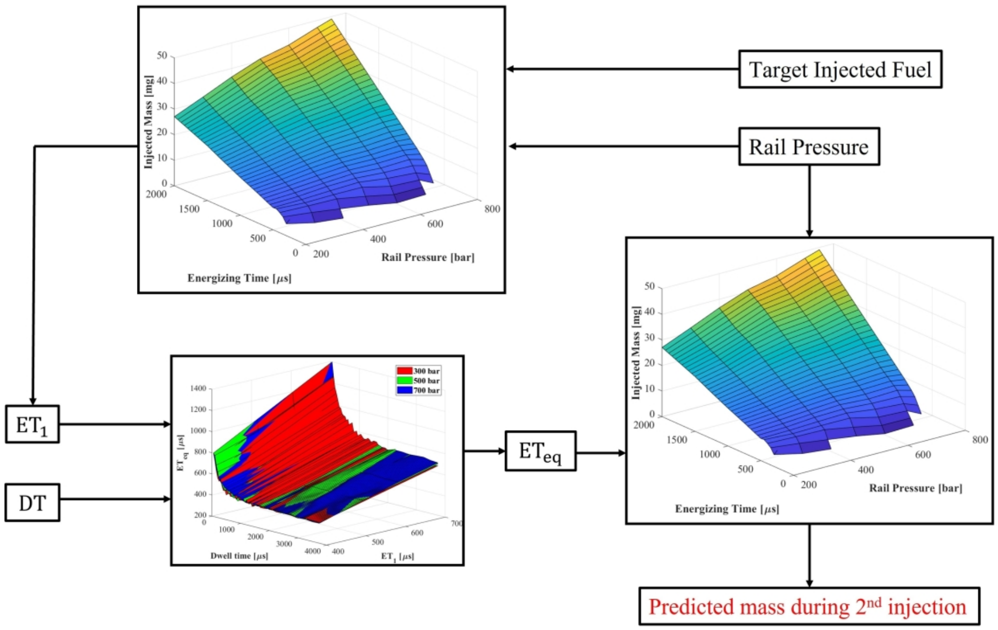

Figure 18: Procedure for the model validation.

280x180mm (300 x 300 DPI)

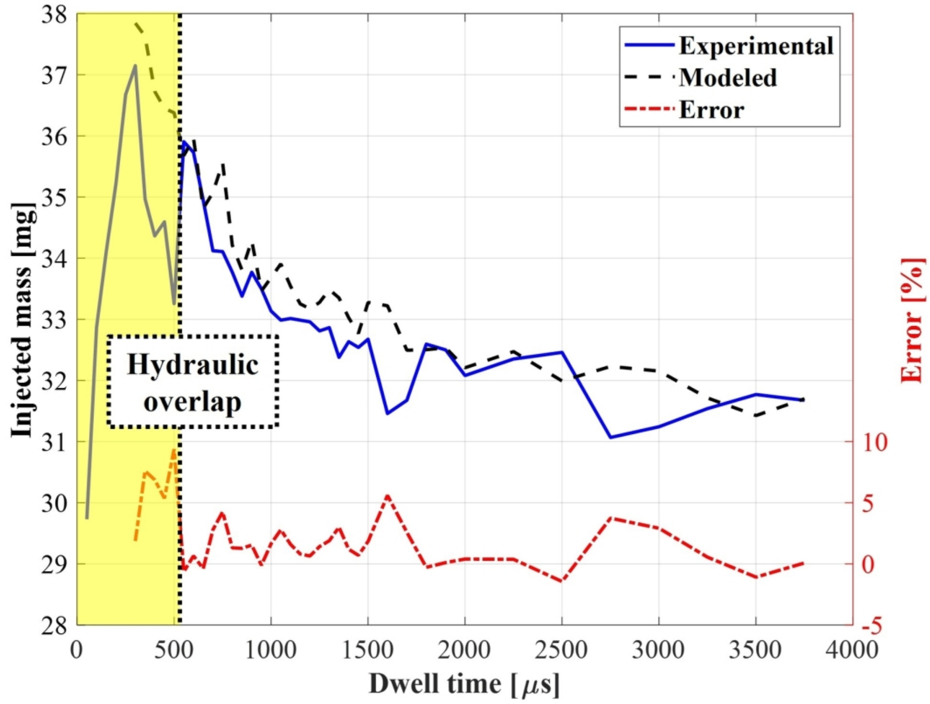

Figure 19: Comparison between estimated and experimental injected mass for 300 bar of injection pressure and ET_1=700 µs.

161x120mm (300 x 300 DPI)

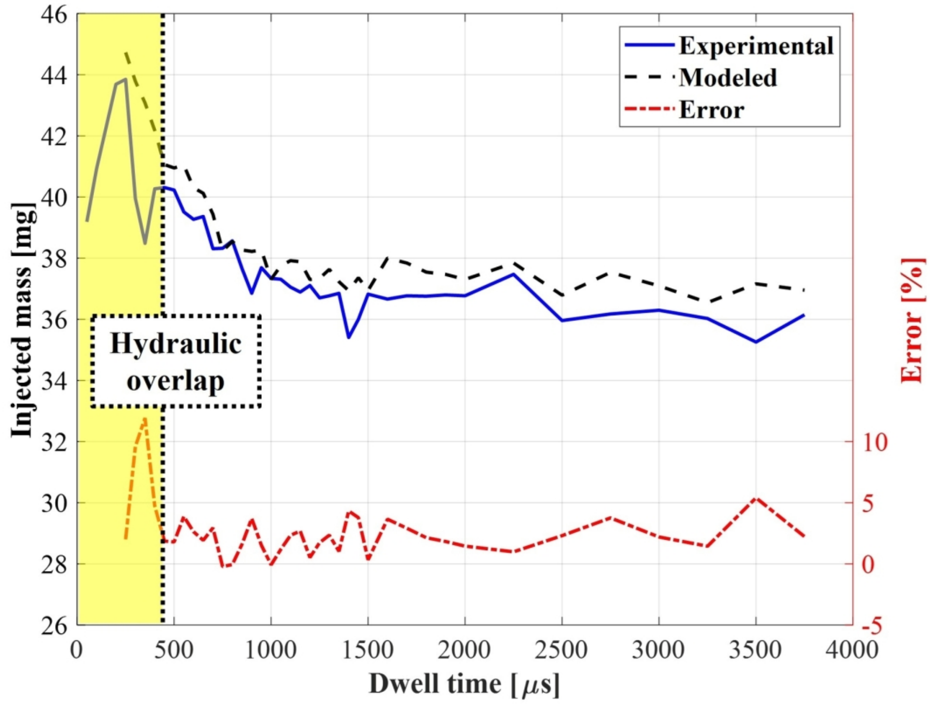

Figure 20: Comparison between estimated and experimental injected mass for 500 bar of injection pressure and ET_1=700 μs.

161x120mm (300 x 300 DPI)

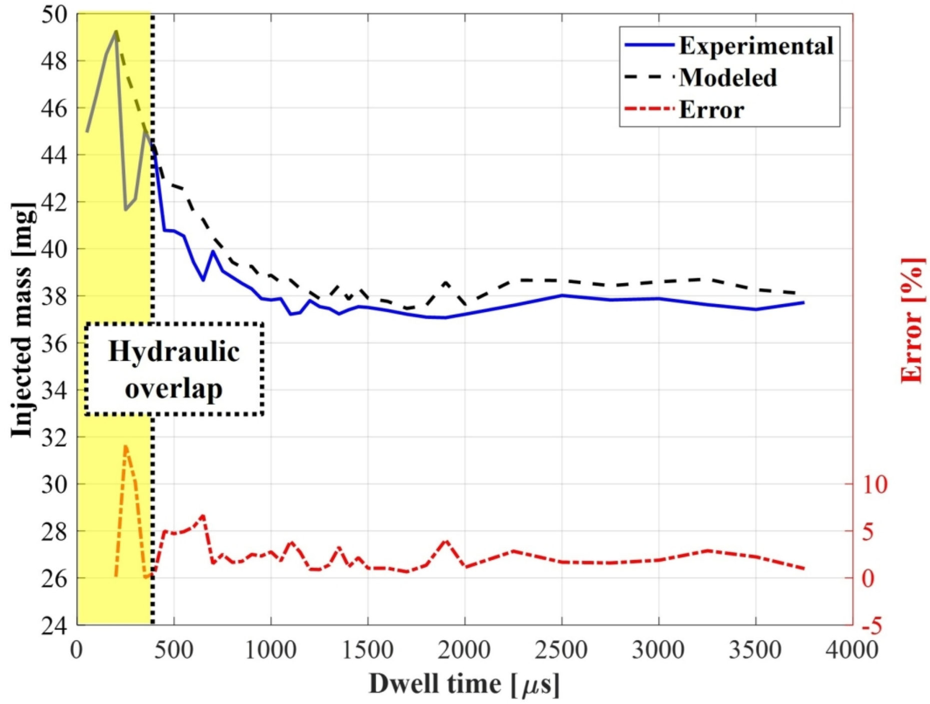

Figure 21: Comparison between estimated and experimental injected mass for 700 bar of injection pressure and ET_1=700 μs.

161x120mm (300 x 300 DPI)

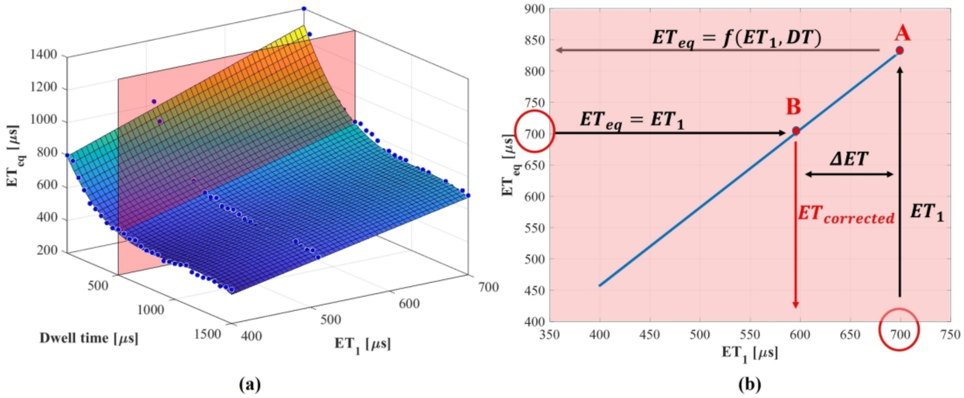

Figure 22: (a) Fitted surface for ET_eq and interception with the red plane at DT=500 μs;
(b) Explanation of the increased ET if ET_1=ET_2 (point A) and determination of the corrected ET (point B).

258x110mm (300 x 300 DPI)

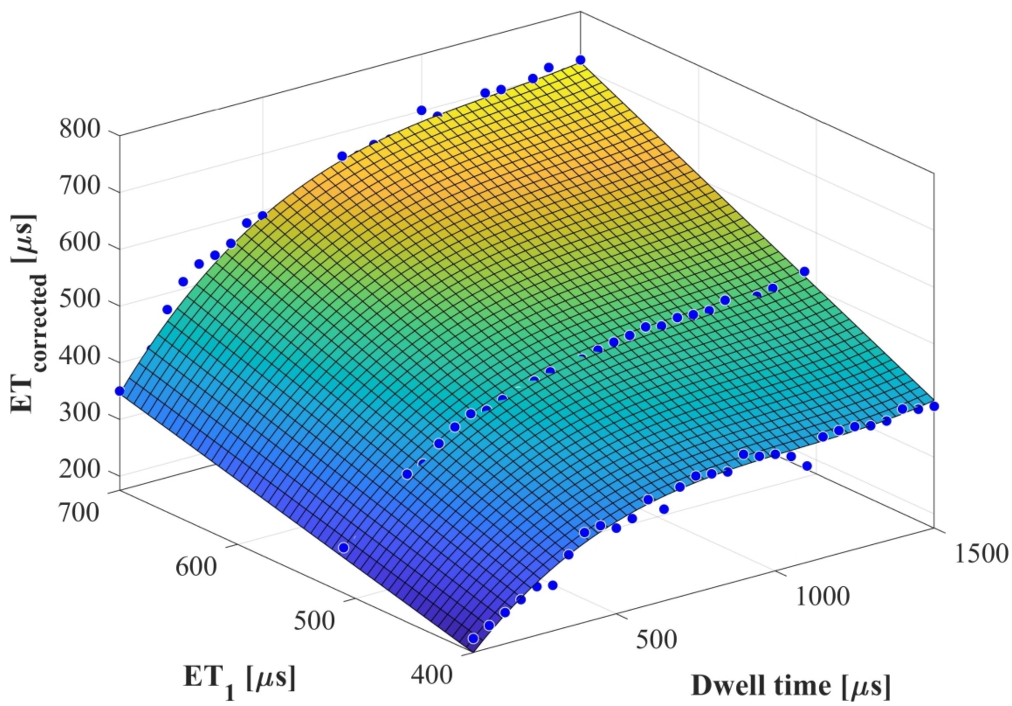

Figure 23: Map for the corrected ET.

839x582mm (72 x 72 DPI)

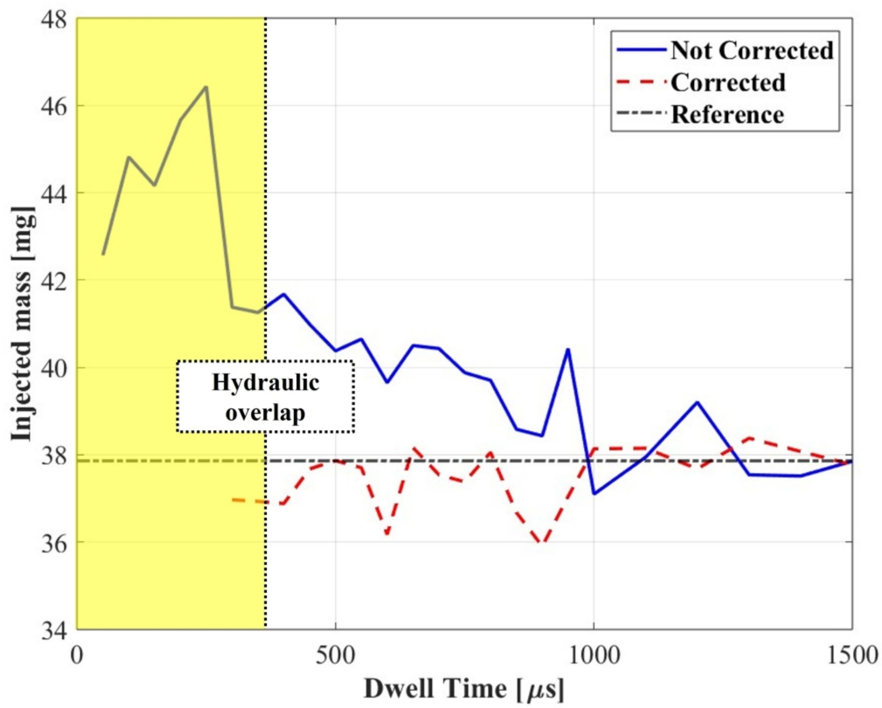

Figure 24: Comparison between not corrected and corrected fuel injected mass with 500 bar injection pressure and ET_1=700 µs.

254x190mm (300 x 300 DPI)

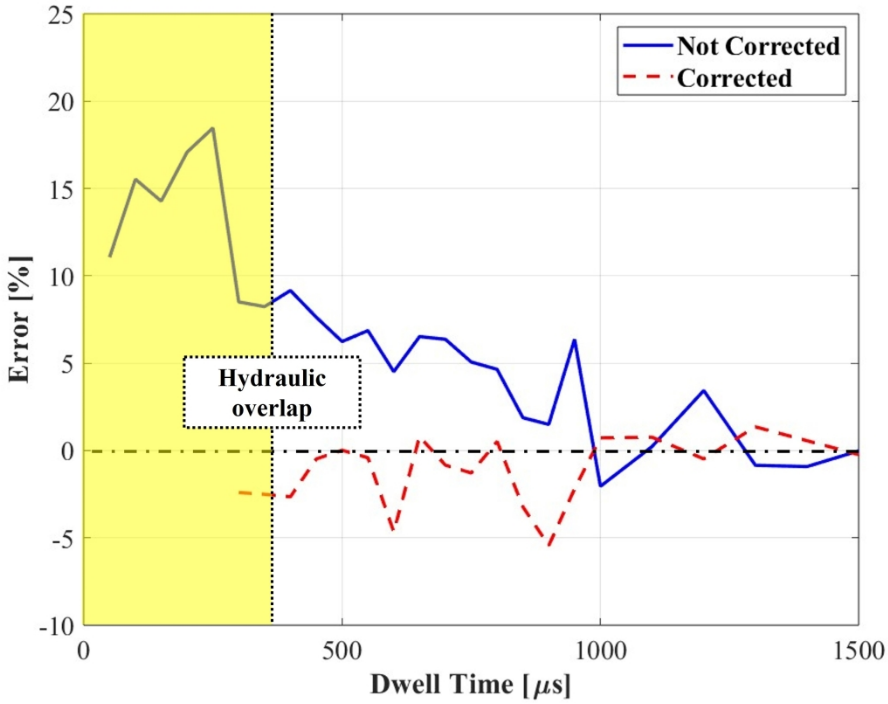

Figure 25: Comparison between the error of not corrected and corrected fuel injected mass with 500 bar injection pressure and ET_1=700 μs.

254x190mm (300 x 300 DPI)

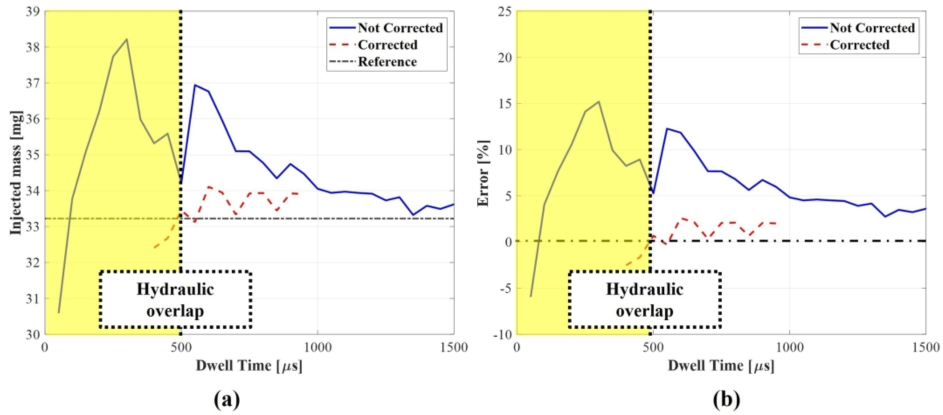

Figure 26: (a) Comparison between not corrected and corrected fuel injected mass with 300 bar injection pressure and ET_1=700 μs; (b) Comparison between the error of not corrected and corrected fuel injected mass with 300 bar injection pressure and ET_1=700 μs.

214x95mm (300 x 300 DPI)

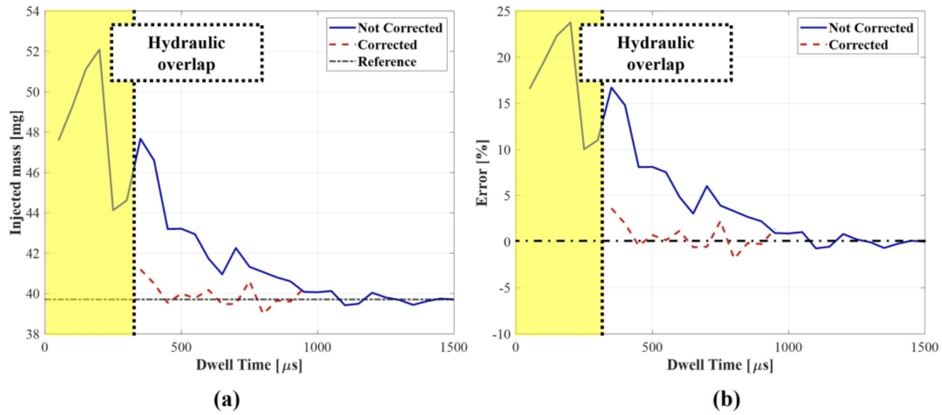

Figure 27: (a) Comparison between not corrected and corrected fuel injected mass with 700 bar injection pressure and ET_1=700 μs; (b) Comparison between the error of not corrected and corrected fuel injected mass with 700 bar injection pressure and ET_1=700 μs.

214x95mm (300 x 300 DPI)